PALEOCEANOGRAPHY, VOL. 18, NO. 4, 1097, doi:10.1029/2003PA000909, 2003

Orbital climate forcing of $\delta^{13}C$ excursions in the late Paleocene–early Eocene (chrons C24n–C25n)

Benjamin S. Cramer,[1,2] James D. Wright,[1] Dennis V. Kent,[1,3] and Marie-Pierre Aubry[1]

Received 4 April 2003; revised 12 August 2003; accepted 22 September 2003; published 18 December 2003.

[1] High-resolution stable carbon isotope records for upper Paleocene–lower Eocene sections at Ocean Drilling Program Sites 1051 and 690 and Deep Sea Drilling Project Sites 550 and 577 show numerous rapid (40–60 kyr duration) negative excursions of up to 1‰. We demonstrate that these transient decreases are the expected result of nonlinear insolation forcing of the carbon cycle in the context of a long carbon residence time. The transients occur at maxima in Earth's orbital eccentricity, which result in high-amplitude variations in insolation due to forcing by climatic precession. The construction of accurate orbital chronologies for geologic sections older than ~35 Ma relies on identifying a high-fidelity recorder of variations in Earth's orbital eccentricity. We use the carbon isotope records as such a recorder, establishing a robust orbitally tuned chronology for latest Paleocene–earliest Eocene events. Moreover, the transient decreases provide a means of precise correlation among the four sites that is independent of magnetostratigraphic and biostratigraphic data at the $<10^5$-year scale. While the eccentricity-controlled transient decreases bear some resemblance to the much larger-amplitude carbon isotope excursion (CIE) that marks the Paleocene/Eocene boundary, the latter event is found to occur near a minimum in the ~400-kyr eccentricity cycle. Thus the CIE occurred during a time of minimal variability in insolation, the dominant mechanism for forcing climate change on 10^4-year scales. We argue that this is inconsistent with mechanisms that rely on a threshold climate event to trigger the Paleocene/Eocene thermal maximum since any threshold would more likely be crossed during a period of high-amplitude climate variations. *INDEX TERMS:* 1620 Global Change: Climate dynamics (3309); 1520 Geomagnetism and Paleomagnetism: Magnetostratigraphy; 4267 Oceanography: General: Paleoceanography; 1040 Geochemistry: Isotopic composition/chemistry; 3030 Marine Geology and Geophysics: Micropaleontology; *KEYWORDS:* carbon isotopes, orbital stratigraphy, Paleocene/Eocene boundary

Citation: Cramer, B. S., J. D. Wright, D. V. Kent, and M.-P. Aubry, Orbital climate forcing of $\delta^{13}C$ excursions in the late Paleocene–early Eocene (chrons C24n–C25n), *Paleoceanography*, *18*(4), 1097, doi:10.1029/2003PA000909, 2003.

1. Introduction

1.1. Background

[2] The Paleocene/Eocene (P/E) boundary (~55 Ma) is characterized by a transient 2–5‰ decrease in marine and terrestrial carbon isotope ($\delta^{13}C$) records [*Kennett and Stott*, 1991; *Koch et al.*, 1992]. The onset of this carbon isotope excursion (CIE) occurred in <50 kyr, followed by an exponential recovery to pre-excursion values over ~150 kyr [*Katz et al.*, 1999; *Norris and Röhl*, 1999; *Röhl et al.*, 2000]. It was accompanied by an equally abrupt excursion to extremely low $\delta^{18}O$ values in marine records, indicating that global temperatures exceeded those recorded at any other time during the Cenozoic and leading to the designation of the event as the Paleocene/Eocene thermal maximum (PETM; formerly latest Paleocene thermal maximum). Extensive research has concentrated on the ~200 kyr interval containing the perturbation and subsequent recovery of geochemical proxies during the PETM at numerous locations [e.g., *Kennett and Stott*, 1991; *Koch et al.*, 1992; *Zachos et al.*, 1993; *Koch et al.*, 1995; *Bralower et al.*, 1995; *Kaiho et al.*, 1996; *Schmitz et al.*, 1996; *Stott et al.*, 1996; *Thomas and Shackleton*, 1996; *Bralower et al.*, 1997; *Bains et al.*, 1999; *Cramer et al.*, 1999; *Katz et al.*, 1999; *Norris and Röhl*, 1999; *Thomas et al.*, 1999; *Röhl et al.*, 2000; *Bowen et al.*, 2001] but relatively little effort has been made to place the event in a longer-term context. It has been well documented that the PETM occurred in the middle of a ~7 myr-long warming trend, and that global $\delta^{13}C$ values also decreased over a ~4 myr interval (Figure 1; *Miller et al.* [1987]; *Zachos et al.* [2001a]), but it is not known whether these long-term changes occurred monotonically or may have been punctuated by intervals of rapid climate change on timescales <1 myr

[3] Our primary objective in this study is to provide a framework for more detailed study of the long-term climate change during the latest Paleocene to earliest Eocene. Since variations in the geometry (precession, obliquity, and eccentricity) of Earth's orbit around the sun have been recognized as a primary driver of climate change on timescales

[1]Department of Geological Sciences, Rutgers University, Piscataway, New Jersey, USA.
[2]Now at Institute of Geology and Paleontology, Tohoku University, Sendai, Japan.
[3]Also at Lamont-Doherty Earth Observatory, Palisades, New York, USA.

0883-8305/03/2003PA000909$12.00

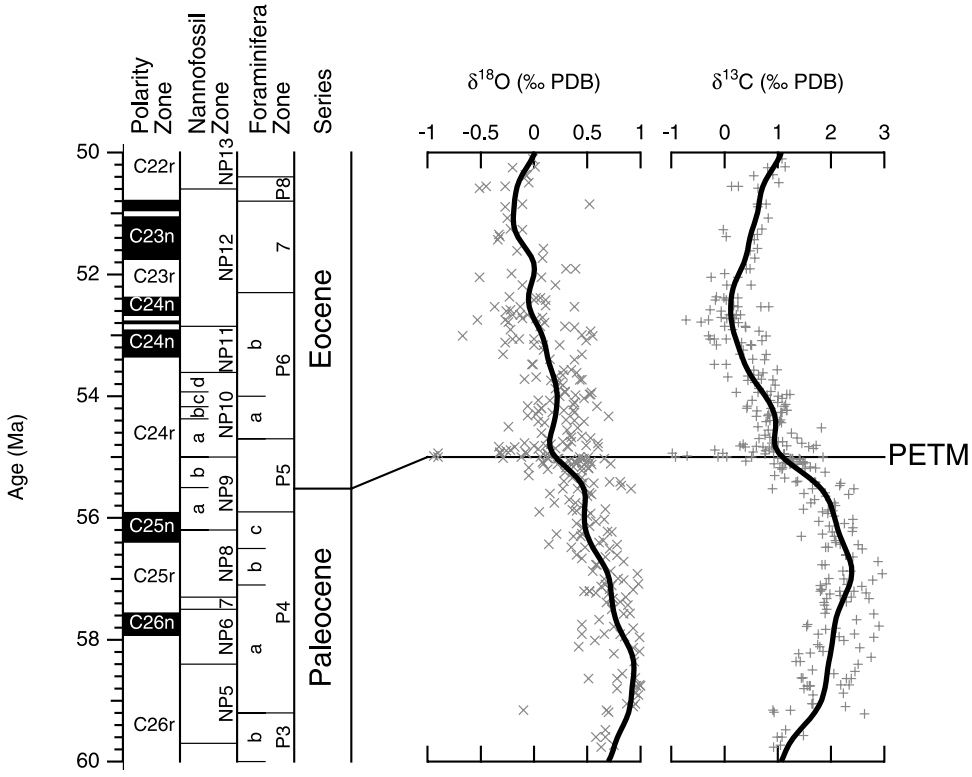

Figure 1. Latest Paleocene–earliest Eocene integrated magnetobiochronology of *Berggren et al.* [1995], modified following *Aubry et al.* [1996], *Aubry* [1996], *Aubry and Sanfilippo* [1999], and *Aubry et al.* [2002], shown with a global synthesis of benthic foraminiferal stable isotope measurements. Note that the isotope synthesis and magnetobiochronology are plotted on slightly different timescales; the isotope synthesis is plotted according to a modified timescale that uses an age of 55 Ma for the PETM (*Zachos et al.* [2001a] following *Norris and Röhl* [1999]), although this level is equivalent to the NP9a/b boundary which was assigned an age of 55.52 Ma by *Aubry et al.* [1996]. Data points shown are actual measured values rather than the presmoothed data that are plotted in the work of *Zachos et al.* [2001a] (data taken from J.C. Zachos's Web site: http://www.es.ucsc.edu/%7Esilab/ZACPUBDATA/2001CompilationData.txt). Smoothed heavy line through the isotope data was calculated using a Gaussian filter with a cutoff (20% response) at a period of 1 myr.

$<10^6$ years [e.g., *Hays et al.*, 1976; *Olsen and Kent*, 1996; *Lourens and Hilgen*, 1997; *Maslin et al.*, 1998; *Olsen and Kent*, 1999; *Shackleton*, 2000; *Zachos et al.*, 2001b], the framework we present is a cyclostratigraphic one (we use the term "cyclostratigraphy" in this work to refer to cyclicity presumed to reflect orbital forcing of climate). However, our approach departs from that of previous cyclostratigraphic studies in this time period [e.g., *Norris and Röhl*, 1999; *Katz et al.*, 1999; *Cramer*, 2001; *Röhl et al.*, 2000; *Dinarès-Turell et al.*, 2002] in that we concentrate on identification of the longer-period eccentricity variations rather than precession cycles. We emphasize the construction of a cyclostratigraphic framework that is applicable in sections with poorly developed lithologic cyclicity (e.g., Sites 550 and 577) and is useful for correlation among widely separated locations as well as for calibration of durations at a single site.

[4] A secondary objective is to test the possibility that orbital (Milankovitch) forcing of climate somehow triggered the PETM climatic perturbation, possibly by providing the final push that drove the climate system past some critical threshold. There is good evidence that gradual tectonic change can result in rapid climate change as the climate system is forced across some critical physical threshold, but that the timing of the ultimate crossing of that threshold occurs as a result of orbital forcing. For instance, high amplitude climate variations resulting from modulation of precession and obliquity cyclicity have been implicated in the intensification of Neogene glaciations [*Lourens and Hilgen*, 1997; *Maslin et al.*, 1998; *Zachos et al.*, 2001b, 2001a]. In their description of the PETM, *Kennett and Stott* [1991] noted that the event occurred superposed on the long-term late Paleocene–early Eocene warming trend. They hypothesized that it represented a rapid transition between climate states due to the crossing of some critical climate threshold that triggered an ocean circulation change, shifting deepwater formation from high to low latitudes. This basic hypothesis has subsequently been elaborated to explain the CIE through release of ^{12}C-enriched methane as the switch to warmer low-latitude-sourced deep/intermediate waters resulted in the melting of methane hydrates [*Dickens et al.*,

1995; *Bralower et al.*, 1997; *Dickens et al.*, 1997; *Bains et al.*, 1999; *Zachos et al.*, 2001a]. More recently, it has been suggested that subduction of warmer surface waters for ~1.7 kyr prior to the CIE resulted in dissociation of methane hydrate and initiated a feedback loop as methane released into the atmosphere resulted in further global warming [*Thomas et al.*, 2002]. Although, to our knowledge, it has not previously been suggested that the timing of the PETM may have been related to high-amplitude variations in insolation that would be expected to occur at eccentricity maxima, we believe that orbital forcing is an obvious source of climate change on timescales relevant to the initiation of this event and that the temporal placement of the PETM relative to eccentricity variations is of fundamental importance in identifying the ultimate cause of the event.

1.2. Upper Paleocene–Lower Eocene Stratigraphy and Correlation

[5] Correlation and temporal calibration of events surrounding the Paleocene/Eocene (P/E) boundary has proven to be a particularly thorny problem in chronostratigraphy, in large part due to the boundary's placement within the ~2.5-myr-long reversed polarity interval of magnetic polarity chron C24r, the second longest polarity chron in the Cenozoic (Figure 1). A primary basis for converting lithologic thicknesses to numerical chronologies has been the identification of magnetic reversals, which have been dated by assuming smoothly varying seafloor spreading rates between radiometrically dated tie-points in the South Atlantic [*Cande and Kent*, 1992a, 1995]. By default, correlation among sites within the interval of chron C24r has been dependent on the identification of biostratigraphic events and the assumption of their synchrony at all sites, while their numerical calibration has been dependent on assumptions of constant sedimentation rates during parts of chron C24. On these bases, *Berggren and Aubry* [1996] and *Aubry et al.* [1996] established a provisional numerical chronology for the P/E boundary interval using a composite section of ODP Site 690 for early chron C24r and DSDP Site 550 for late chron C24r and chron C24n. On the basis of this composite section, they estimated an age for the CIE of 55.52 Ma relative to the timescales of *Cande and Kent* [1992a, 1995] and *Berggren et al.* [1995], or 0.38 myr following the C24r/C25n reversal.

[6] Cyclostratigraphy provides an alternate method for timescale calibration not reliant on interpolation of either seafloor spreading or sedimentation rates or on assumptions of synchrony of biostratigraphic datums [e.g., *Hilgen*, 1991a, 1991b; *Shackleton et al.*, 1990, 2000]. *Norris and Röhl* [1999] presented the first attempt at a cyclostratigraphic calibration of the age of the CIE based on counting presumed precessional cycles up from the base of Magnetozone C24r at ODP Site 1051 and assuming a mean precession period of 0.021 myr They concluded that the CIE occurred 0.924–0.966 myr following the C24r/C25n polarity reversal, which implies an age of ~54.96 Ma relative to the *Cande and Kent* [1992a, 1995] GPTS. *Cramer* [2001] investigated using the same methodology of cycle counting to refine the calibration of biostratigraphic datums within chron C24r and produced a biocyclostratigraphic correlation between Sites 1051 and 690. However, *Cramer* [2001] demonstrated that the error inherent in precessional cycle recognition is too large to allow any real test either of the *Cande and Kent* [1992a, 1995] calibration or of the assumption of minimal biostratigraphic diachrony.

1.3. Rationale for Our Approach to Cyclostratigraphy

[7] Variations in Earth's orbit result from gravitational interactions between the celestial bodies in the solar system. These result in cyclic variations in the distribution of insolation on Earth's surface due to climatic precession (wobble of Earth's axis relative to the ellipse of Earth's orbit; ~19 and ~23 kyr periods) and variations in obliquity (tilt of the orbital plane relative to Earth's axis of rotation; ~41 kyr period). The amplitude of the precessional insolation variations is modulated by variations in the eccentricity of Earth's orbit (~100, ~400, and ~2400 kyr periods; we will henceforth refer to these as short, long, and very long eccentricity components, respectively). The periods cited here are only the primary ones of many that influence Earth's climate; in fact, chaotic interactions prevent a completely accurate characterization of the behavior of the solar system using a summation of periodic components [e.g., *Laskar*, 1999].

[8] Geologic records that are assumed to reflect orbital variations can be differentially stretched in order to match a calculated record of orbital variations. Under the assumption that differences between the geologic and calculated records reflect varying sedimentation rates, "tuning" algorithms take a record plotted relative to geologic thickness and an orbitally based target curve as input and output a sedimentation rate curve (see *Shackleton et al.* [1999] for a good description of tuning in practice). For the late Neogene, "orbital" or "astro-" chronologies based on tuning the geologic record to numerically calculated variations in insolation forced by variations in precession and obliquity have superseded radioisotope geochronology and the seafloor spreading-based GPTS as the basis for assigning numerical ages to geologic events [*Hilgen*, 1991a, 1991b; *Shackleton et al.*, 1990, 1999, 2000]. However, *Laskar* [1990, 1999] demonstrated that uncertainties in knowledge of the present configuration of the solar system in the context of the chaotic behavior of the inner solar system limit accurate calculations of the orbital and precessional motion of the Earth to the time period <35 Ma. *Berger et al.* [1992] further noted that the gradual increase in the Earth-moon distance and length of the day results in uncertainties in the fundamental periods of obliquity and precession that are larger than the uncertainties due to chaotic interactions.

[9] In contrast, short and long eccentricity periods can be considered to remain constant through time, and *Laskar* [1999] and *Berger et al.* [1992] concluded that recognition of eccentricity variations in the geologic record should be used as the basis for construction of orbital chronologies for time periods >30 Ma. This approach has been used to generate an accurate timescale for more than 25 myr of Upper Triassic lacustrine sequences [e.g., *Olsen and Kent*, 1996, 1999] and as a supplement to precession and obliquity cycle-recognition for upper Paleogene–Neogene marine sediments [e.g., *Hilgen*, 1991b]. In general, though, the imprint of eccentric-

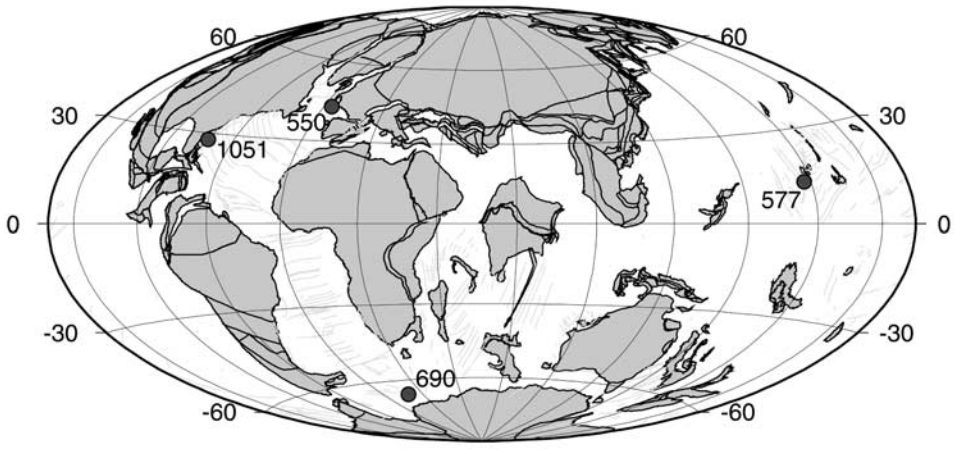

Figure 2. Early Paleogene paleogeographic reconstruction showing the location of the four sites used in this study. Reconstruction made using the Web-based software available at http://www.odsn.de/odsn/services/paleomap/paleomap.html [*Hay et al.*, 1999]. See color version of this figure in the HTML.

ity on marine lithologic variations is subtle, resulting in amplitude variations of the ~21 kyr (precession) component of the signal that can be observed only after the record has been tuned and variations at other frequencies have been removed using a bandpass filter [e.g., *Shackleton et al.*, 1999]. In an untuned and unfiltered lithologic record, it is difficult to confidently identify the eccentricity modulation because of sedimentation rate changes as well as the frequent presence of obliquity-forced variations.

1.4. Eccentricity in $\delta^{13}C$ Records

[10] Our approach is inspired by the idea that we may be able to bypass the problems inherent in the recording mechanism (sediment deposition) by taking advantage of certain natural processes that can act as real-time low-pass filters of the signal being recorded. Any natural process that has a "memory" (i.e., the past state of the process affects the present state) effectively reduces the amplitude of rapid fluctuations in forcing and preserves more gradual changes, similar to the effect of numerical low-pass filters. In particular, marine $\delta^{13}C$ variations are subject to a low-pass filter due to the residence time of carbon: much of the carbon in the ocean-atmosphere-biosphere reservoir has been there for 10^5 years, so the current $\delta^{13}C$ value reflects the composition in the past as well as more recent changes in the carbon cycle.

[11] High-amplitude (~1‰) eccentricity-controlled cyclicity has been described in various upper Paleogene–Neogene (<30 Ma) $\delta^{13}C$ records [*Woodruff and Savin*, 1991; *Flower and Kennett*, 1995; *Diester-Haass*, 1996; *Zachos et al.*, 1996, 1997], suggesting that carbon isotope records may be useful for constructing eccentricity-based orbital chronologies for older marine strata. We also emphasize that eccentricity-scale variations in $\delta^{13}C$ values should be correlative among sites at 10^3-year timescales since this is the mixing time for carbon through the ocean-atmosphere-biosphere reservoir [*Broecker and Peng*, 1982; *Siegenthaler and Sarmiento*, 1993; *Sarmiento and Bender*, 1994]. We therefore employ a new strategy using $\delta^{13}C$ records to provide a firm orbital timescale of the chron C24n.3n–C25n interval as well as high-resolution (<100 kyr) correlation among geographically distant sites.

2. Data Collection and Description

2.1. Material

[12] We analyzed material from four sites: Deep Sea Drilling Project (DSDP) Sites 550 and 577 and Ocean Drilling Program (ODP) Sites 690 and 1051 (all new data are available in electronic format in the online auxiliary material[1]). The sites were chosen based on two primary considerations:

[13] 1. These sites provide the global geographic coverage needed to demonstrate the correlation potential of eccentricity cycle recognition in $\delta^{13}C$ records (Figure 2). Of the four sites, two are in the North Atlantic Ocean (DSDP Site 550 and ODP Site 1051), one is in the Southern Ocean (ODP Site 690), and one is in the Pacific Ocean (DSDP Site 577).

[14] 2. These sites have provided the basis for previous early Paleogene temporal calibrations. Sites 690 and 550 were used by *Berggren and Aubry* [1996] and *Aubry et al.* [1996] to establish a provisional latest Paleocene–earliest Eocene chronology. The chron C24r magnetostratigraphy for this interval at Sites 550 and 577 is fairly clean and, as a consequence, these sites were used for many of the biochronologic calibrations in the work of *Berggren et al.* [1995]. Sites 1051 and 690 were used in previous late Paleocene–early Eocene cyclostratigraphic studies [*Norris and Röhl*, 1999; *Katz et al.*, 1999; *Röhl et al.*, 2000; *Cramer*, 2001] and preliminary magnetostratigraphic studies for Site 1051 were promising [*Ogg and Bardot*, 2001].

2.2. Nannofossil Biostratigraphy

[15] Occurrences of calcareous nannofossil marker species were taken from published reports for Sites 550 [*Muller*, 1985; *Berggren and Aubry*, 1996; *Aubry et al.*, 1996], 577 [*Aubry*, 1998], 690 [*Pospichal and Wise*, 1990;

[1] Auxiliary material is available at ftp://ftp.agu.org/apend/pa/2003PA000909.

Berggren and Aubry, 1996; *Aubry et al.*, 1996], and 1051 [*Mita*, 2001]. Additional samples from Holes 1051A and 1051B were examined for this study. Biozonal subdivisions follow the (sub)zonal scheme of *Martini* [1971]; *Aubry* [1996], and *Aubry and Sanfilippo* [1999]. Nannofossil stratigraphy was used in preference to planktonic foraminiferal stratigraphy because the former is more refined than the latter at most sites. Also, the midlatitude foraminiferal biozonal scheme is not applicable at Site 690 [*Stott and Kennett*, 1990], preventing direct intersite comparison.

2.3. Magnetostratigraphy

[16] Interpreted magnetic polarity stratigraphies were taken from published reports for Sites 550 [*Ali and Hailwood*, 1998; *Townsend*, 1985], 577 [*Bleil*, 1985], and 690 [*Ali et al.*, 2000]. A preliminary magnetostratigraphic study for Site 1051 [*Ogg and Bardot*, 2001] produced promising results, but only samples from Hole 1051A were progressively demagnetized and the sample spacing was coarse. We analyzed 214 samples from Holes 1051A and 1051B to better constrain the magnetostratigraphy. Samples were cut to fit in standard ODP cubes (7 cc) by staff at the ODP core repository in Bremen. Natural remanent magnetism (NRM) was measured on a 2G DC SQUID 3-axis cryogenic magnetometer housed in a magnetically shielded room at Lamont-Doherty Earth Observatory. Step demagnetization of NRM at 5–10 mT increments to 45 mT was performed using a large-volume alternating field (AF) demagnetization coil. Further demagnetization using a single-specimen AF demagnetization coil was attempted for some samples but did not yield useful results. Despite the presence of a magnetic overprint, we believe that the magnetic polarity stratigraphy obtained for Site 1051 is reliable based on the good correspondence of reversals between Holes 1051A and 1051B, the consistency of the reversal pattern with the GPTS for this time interval, and the correlations with the calcareous nannofossil stratigraphy (Figures 3–5; more information is available in the online auxiliary material[1]).

2.4. Carbon Isotopes

[17] We sampled for bulk carbonate $\delta^{13}C$ analysis from Holes 690B, 1051A, 1051B, 550, and 577 at an interval sufficient to provide temporal resolution of ~20 kyr throughout the sections and ~4 kyr for large portions of them. Relatively large (~1 cc) samples were taken so that possible contamination on the cut surface of the core could be avoided by analyzing subsamples from the interior of the core. Isotope analysis was performed at Rutgers University. Bulk sediment subsamples (1–10 mg) were reacted in phosphoric acid (H_3PO_4) at 90°C in a Multiprep peripheral attached to a Micromass Optima mass spectrometer. The analytical precision (2 σ) of the standards analyzed (either NBS19 or an in-house standard referenced to NBS19) was <0.04‰ ($\delta^{13}C$) for each sample run; reproducibility of sample analyses between runs was typically within the analytical precision.

[18] Variations in the $\delta^{13}C$ record in all five sections show major features that are correlatable between sections (Figures 3–5). The good correlation implies that these features (the primary source of our interpretation) essentially reflect variations in the $\delta^{13}C$ value of the oceanic inorganic carbon reservoir rather than local effects. We recognize that the interpretation of bulk carbonate isotopic analyses can be compromised by a combination of factors including changes in nannofossil species composition, changes in the size distribution of planktonic foraminifera, and diagenesis. With the exception of the interval below the CIE at Site 550, we do not believe that our interpretations are significantly compromised by these factors. We suspect that the $\delta^{13}C$ record in the interval below ~410 mbsf at Site 550 (Figure 5) is significantly affected by the presence of postdepositional carbonate precipitation resulting from the breakdown of organic matter and consequently having a very low (~−20‰) $\delta^{13}C$ value. Such carbonate is likely to be present in small amounts in all marine sediments, but in general, its contribution to the $\delta^{13}C$ record can be ignored because of the overwhelming dominance of pelagic carbonate. In intervals of low pelagic carbonate preservation, such as the interval below the CIE at Site 550, a significant portion of the carbonate present can be postdepositional. We have entirely excluded from the interpreted data set values <0 (as low as −14) that occur near the onset of the CIE at Site 550 (~410 mbsf) and values from Site 577 for sediments at the top of core 10 (~83 mbsf), which was severely disturbed during drilling and contains Pleistocene nannofossils [*Aubry*, 1998]; these values can be found in the archived data tables in the online auxiliary material[1].

[19] The most prominent feature of the $\delta^{13}C$ records is the 2.5‰ decrease at the P/E boundary: the CIE (Figure 4). Several similar, albeit lower amplitude (0.5–1.0‰), transient decreases occur at the two ends of the interval (within chron C24n and below the CIE), whereas the sections immediately above the CIE are characterized by variations of <0.5‰ (Figures 3–5). For ease of discussion, we have labeled transient decreases discussed in the text (and subsequently interpreted as reflecting long eccentricity maxima) with the letters A-L in each figure; paired transients are individually identified with a 1 or 2 following the letter. Relative to the magnetobiostratigraphy at each site, the 0.5–1.0‰ transient decreases at the top and bottom of the studied interval correlate well among the four sites. In particular:

[20] 1. A ~1‰ transient decrease (H1) followed immediately by a lower amplitude transient (H2) occurs between the base of Zone NP11 and the base of Magnetozone C24n at Sites 1051 (Hole 1051A), 550, and 577 (Figure 3). A >1‰ transient also occurs at Site 690 immediately above the NP10/NP11 zonal boundary (Figure 3). We correlate it with the lower of the two transients (H1) at the other sites. The magnetostratigraphy in this interval is questionable at Site 690 [see *Ali et al.*, 2000], and a series of unconformities immediately above this transient (H1) has been inferred from the close occurrences of the NP10/NP11, NP11/NP12, and NP12/NP14 contacts (Figure 4; see *Berggren and Aubry* [1996] and *Aubry et al.* [1996]).

[21] 2. A pair of transient events (I1 and I2) occurs within the lowermost normal subchron of chron C24n at Sites 1051 (Hole 1051A), 550, and 577 (Figure 3).

[22] 3. A pair of transient events (C1 and C2) occurs immediately above the base of C24r at Sites 1051 and 690, although this interval is compromised by poor core recovery

at Site 690 (Figure 5). The $\delta^{13}C$ record is compromised in this interval at Site 550 by very low carbonate content and at Site 577 by poor core preservation; correlative transients were picked at both sites but with a lower degree of confidence than for Sites 690 and 1051.

[23] 4. A pair of transient events (B1 and B2) occurs within chron C25n at Sites 1051, 577, and 690 (Figure 5).

2.5. Geophysical Logs

[24] Sediment color logs were generated for all sites from core photographs using a modification of the method described in the work of *Cramer* [2001] (procedure file for WaveMetrics Igor Pro is available on request). The principal difference in method is in the postprocessing of the generated color logs. In order to further reduce the effects of lighting variations in the photographs (which principally affect the apparent darkness of the sediment), tristimulus values (red, green, and blue) for Sites 550, 577, and 690 were converted to chromaticity values by normalizing to a grayscale value. The three chromaticity channels were then reduced to a single log by taking the first principal component. This approach was not useful for Site 1051 because the sediment color varies primarily in shades of gray, hence the lighting imparts variations that are not analytically separable from sediment color variations. Instead, the mean of the three tristimulus channels was used. By comparison with shipboard spectrophotometer measurements [*Shipboard Scientific Party*, 1998], we were able to confirm that the artifact introduced by the lighting is minimal at this site [see *Cramer*, 2001].

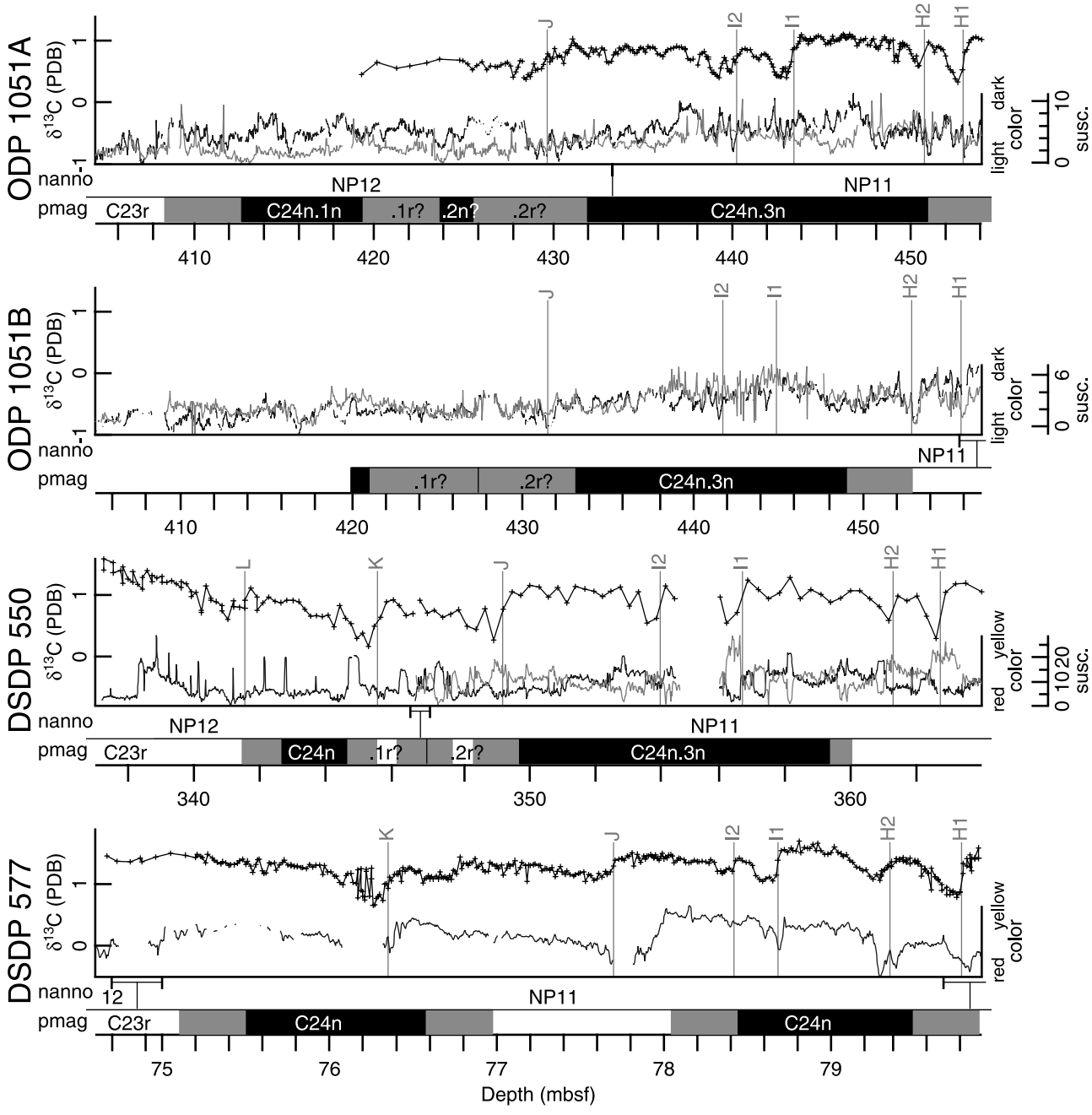

[25] The sediment color logs were supplemented with magnetic susceptibility logs for Sites 1051 [*Shipboard Scientific Party*, 1998], 690, and 550. Magnetic susceptibility logs were generated for Sites 690 and 550 at the ODP East Coast Repository at Lamont-Doherty Earth Observatory using a Bartington MS/2 meter with a MS2F probe capable of obtaining independent measurements at 2 cm intervals.

[26] The final processing step for both color and magnetic susceptibility logs was to subtract a linear trend from each interval of data corresponding to a core section such that the average value in the lower 5 cm of each section matches that in the upper 5 cm of the next section. This procedure was necessary to eliminate pseudo-events resulting from mismatched data values between sections.

[27] The geophysical logs for Sites 690 and 1051 show a robust cyclicity that has been attributed dominantly to precession with some contribution from obliquity at Site 690 [*Cramer*, 2001; *Norris and Röhl*, 1999; *Röhl et al.*, 2000] (Figures 3–5). A less robust cyclicity is present in the logs from Site 550; preliminary cycle counts suggest that the lithologic cyclicity at Site 550 reflects primarily obliquity forcing, but the sedimentary response involves a switch from carbonate to siliceous deposition, imparting an extremely nonlinear response that imperfectly reflects the underlying orbital cyclicity. Sediment color logs from Site 577 are unreliable: although there is a clear cyclicity consistent with precession forcing in some intervals (based on magnetobiostratigraphic sedimentation rate estimates), in other intervals the signal is overwhelmed by the lighting artifact and poor core preservation is a problem throughout (Figures 3–5). However, a longer-wavelength cyclicity consistent with eccentricity forcing is present, suggesting that bioturbation at this site (which has very low sedimentation rates) may have dampened the precessional cyclicity and thereby accentuated eccentricity variations.

3. Construction of the Orbital Timescale

3.1. Background Observations

[28] We take as a starting premise that any orbital tuning is necessarily based on a model for the response of some measured parameter to variations in insolation. Two lines of reasoning are typically used post facto to justify the assumptions inherent to the model: one is the appearance of other orbital periodicities in the tuned records that were not directly used in the tuning process; the other is the appearance of orbital periodicities in other measured parameters not used in the tuning process.

[29] The majority of orbital tuning studies for marine sections have adopted a model that attributes variations in sediment composition (measured using various geophysical or geochemical logs) to a more or less direct forcing by variations in insolation, often at some relatively high latitude so that both precession and obliquity are present in the tuning target (see *Shackleton et al.* [1999] for a thorough discussion of this approach). The actual forcing mechanism is generally a black box: it is rarely modeled in detail but typically involves forcing of productivity, weathering, and deep-water chemistry affecting the carbonate content of the sediment. This approach relies heavily on the accuracy of calculated records of insolation variations, as the insolation record is used directly as the tuning target. Since calculated insolation variations cannot be assumed to be accurate for the early Paleogene [*Laskar*, 1990, 1999; *Berger et al.*, 1992], the sedimentary response model is not well-suited to the present study. We have instead developed a new model that justifies the use of $\delta^{13}C$ records as a target for orbital tuning, exploiting the more stable eccentricity periods rather than precession or obliquity variations. We discuss this method first by emphasizing aspects of the $\delta^{13}C$ records that illustrate the influence of orbital variations and second by presenting a mathematical model that reproduces the principal features of the $\delta^{13}C$ records and is used as the tuning target.

3.2. Indications of an Orbital Imprint on the $\delta^{13}C$ Records

[30] In intervals where the $\delta^{13}C$ records from Sites 1051 and 690 are sampled at sufficiently high resolution ($\sim$4 kyr), there is a fine-scale cyclicity in the $\delta^{13}C$ records that correlates with cyclicity in geophysical logs attributed to precession forcing [*Norris and Röhl*, 1999; *Röhl et al.*, 2000; *Cramer*, 2001] (Figures 3–5 and 6). Although there

Figure 3. (opposite) Carbon isotope, magnetic susceptibility (red/light), and sediment color (blue/dark) data with interpreted calcareous nannofossil biozones and magnetic polarity zones from ODP Holes 690B, 1051A and 1051B, and DSDP Holes 550 and 577. The records are split into three intervals (Figures 3, 4, and 5; see following pages) of approximately 1.5 myr temporal duration. Lettered vertical lines correspond to carbon isotope transient decreases discussed in the text; the line marked CIE corresponds to the base of the carbon isotope excursion and is equivalent to the Paleocene/Eocene boundary. The error in the placement of calcareous nannofossil and magnetic polarity zonal boundaries, due to the sampling interval and nondiagnostic data, is shown by error bars at the top of the line marking nannofossil zonal boundaries and by gray regions for polarity zones. Carbon isotope data plotted as individual points (not connected by lines) are not interpreted for reasons discussed in the text. Breaks in the magnetic susceptibility, sediment color, and $\delta^{13}C$ traces indicate core breaks, lack of recovery, or intervals that could not be sampled. Spacing between tick marks on the depth axes is uneven due to excess recovery and voids. Note that the scale for magnetic susceptibility, sediment color, and $\delta^{13}C$ data changes between Figures 3, 4, and 5, although the range of the $\delta^{13}C$ scale is kept consistent (2.4‰) so that the amplitude of $\delta^{13}C$ variations can be compared. No scale is shown for sediment color data, which is plotted only in relative units. All data were generated for this study except the following: magnetic susceptibility logs for Site 1051 ([*Shipboard Scientific Party*, 1998]); magnetic polarity zonations for Sites 690 [*Ali et al.*, 2000], 550 [*Townsend*, 1985; *Ali and Hailwood*, 1998], and 577 [*Bleil*, 1985]; and nannofossil zonations for Sites 690 [*Pospichal and Wise*, 1990; *Berggren and Aubry*, 1996; *Aubry et al.*, 1996], 550 [*Muller*, 1985; *Berggren and Aubry*, 1996; *Aubry et al.*, 1996], and 577 [*Monechi*, 1985; *Aubry*, 1998]. See color version of this figure in the HTML.

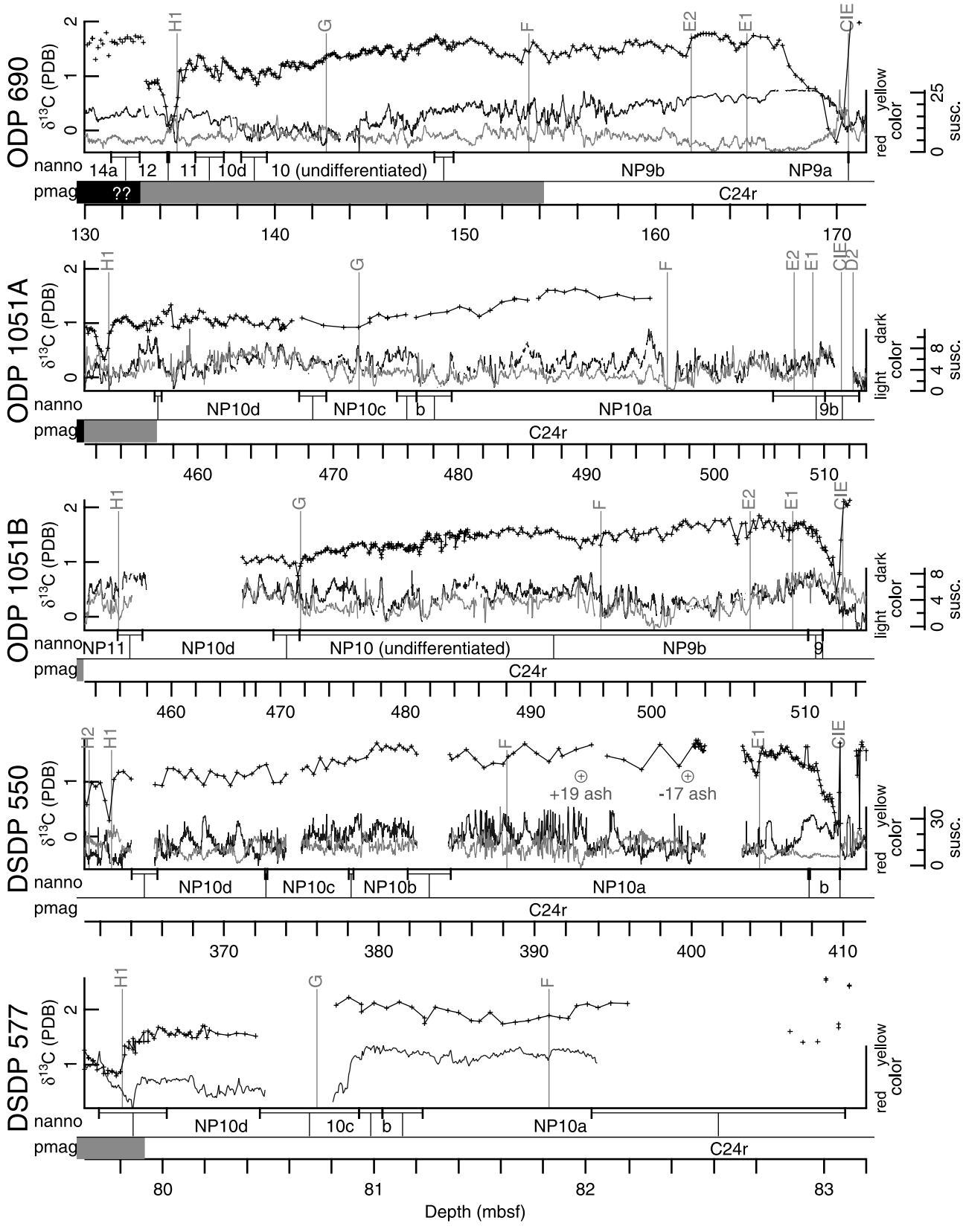

Figure 4. See caption to Figure 3. See color version of this figure in the HTML.

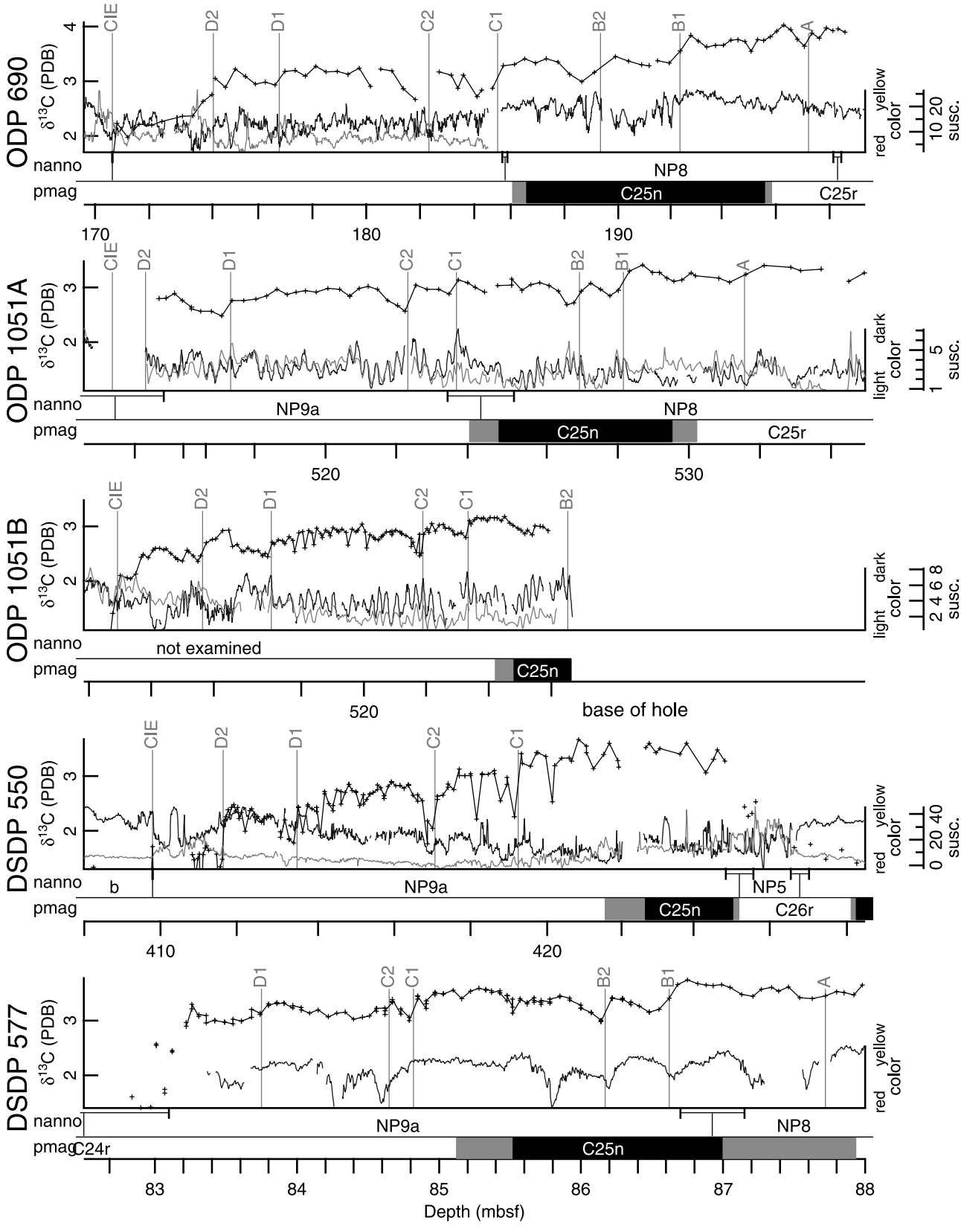

Figure 5. See caption to Figure 3. See color version of this figure in the HTML.

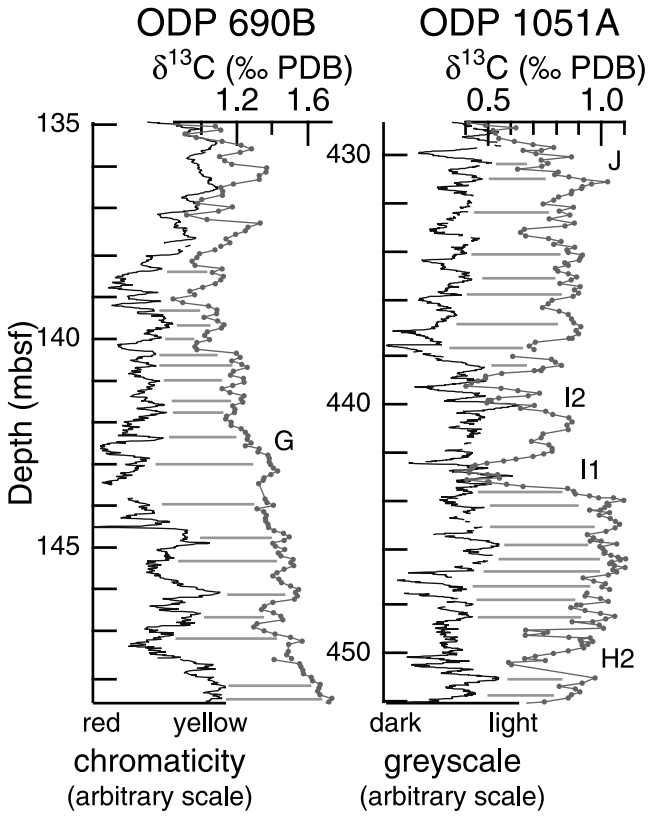

Figure 6. Intervals of $\delta^{13}C$ records from Sites 1051 (right) and 690 (left) sampled at ~4 kyr resolution that display precession-scale cyclicity consistent with cyclicity in sediment color logs. Note that the intervals are not correlative between sites. Horizontal lines are intended as a visual guide and do not demarcate every precessional cycle. Letters next to the $\delta^{13}C$ records refer to transient decreases labeled in Figures 3–5. The records are plotted relative to total core recovery, but depth labels have been adjusted to correspond to ODP standard mbsf. Spacing between tick marks on the depth axis is uneven due to excess recovery and voids. See color version of this figure in the HTML.

is not a one-to-one correlation of cycles between the $\delta^{13}C$ records and the geophysical logs, the match is remarkably good considering that the amplitude of the $\delta^{13}C$ cycles (generally ~0.1‰) is close to the precision of the analyses. Furthermore, in the high-resolution interval above ~455 mbsf in Hole 1051A, which contains high-amplitude transient $\delta^{13}C$ decreases, we also observe a "bundling" of precession cycles into packages of 4–5 cycles delineated by higher-amplitude events, consistent with amplitude modulation by the short eccentricity (~100 kyr) cycle (Figures 3 and 6). This bundling accounts for the closely spaced transient decreases observed in the $\delta^{13}C$ records. Since the interval between paired transients appears to be controlled by short eccentricity modulation, it is likely that the interval from one pair of transients to the next pair reflects amplitude modulation by the long eccentricity (~400 kyr) cycle. This is supported by counting presumed precession cycles in the geophysical logs from Sites 1051 and 690 and assuming a mean precession cycle duration of 21 kyr. The closely spaced transients are separated by 4–6 cycles (84–126 kyr) and the interval from one pair of transients to the next comprises 18–23 cycles (378–483 kyr), consistent with eccentricity periods.

3.3. The $\delta^{13}C$ Model Used as a Tuning Target

[31] Having only this observational evidence that our $\delta^{13}C$ records contain an eccentricity imprint, plus an analogy with Neogene $\delta^{13}C$ records in which the eccentricity signal has been confirmed, it would be difficult to justify tuning the $\delta^{13}C$ records to an eccentricity curve. It might be possible to demonstrate the eccentricity imprint on the carbon isotope records using a cycle-based chronology by simply counting cycles in the geophysical logs. However, *Cramer* [2001] demonstrated that the error associated with cycle recognition is unacceptably large for this method to be reliable. Using such a chronology as a preliminary step would bias our use of the geophysical logs in checking the accuracy of a $\delta^{13}C$-based tuning procedure since the resulting chronology would not be completely independent of the cyclicity in the geophysical logs. On the other hand, using the $\delta^{13}C$ records as the basis for the orbital chronology has the benefit of allowing site-to-site correlation to be integrated into the tuning process.

[32] Because it would be difficult to tune the decidedly nonsinusoidal $\delta^{13}C$ curves using a sinusoidal synthetic eccentricity curve, we sought a mathematical model that would produce a tuning target with similar features to the $\delta^{13}C$ records. The model we use incorporates four assumptions about the early Paleogene carbon cycle:

[33] 1. The ratio of ^{12}C to ^{13}C in marine ΣCO_2 varied as a result of variations in the fraction of total carbon deposited as carbonate or organic carbon, a net increase in organic carbon deposition resulting in increasing $\delta^{13}C$ values for the remaining ΣCO_2, which is reflected in bulk carbonate isotopic measurements.

[34] 2. Low- to midlatitude insolation variations (i.e., precession-dominated) were a significant factor forcing changes in the ratio of carbonate to organic carbon deposition.

[35] 3. The ratio of carbonate to organic carbon deposition was limited from decreasing below some minimum value, for instance due to nutrient limitation of productivity.

[36] 4. The residence time of carbon in the ocean-atmosphere-biosphere reservoir was of order 10^5 years.

[37] The first assumption is commonly used as a conceptual model for interpretation of marine $\delta^{13}C$ records [e.g., [*Miller and Fairbanks*, 1985; *Vincent and Berger*, 1985; *Shackleton*, 1987; *Woodruff and Savin*, 1991; *Flower and Kennett*, 1995; *Zachos et al.*, 1997]. We acknowledge that this model may be overly simplistic [e.g., *Kump and Arthur*, 1999] and that other factors affect the $\delta^{13}C$ signature of ΣCO_2. However, our emphasis is on the net effect of the forcing on global $\delta^{13}C$ variations, which we suppose is primarily driven by the organic/carbonate carbon balance. The second assumption must be true if an eccentricity signal is present in the $\delta^{13}C$ records: eccentricity mainly affects climate through modulation of the precession amplitude. The third assumption results from examination of our data: the transient decreases appear as negative spikes relative to the longer-term changes in $\delta^{13}C$ while rapid positive

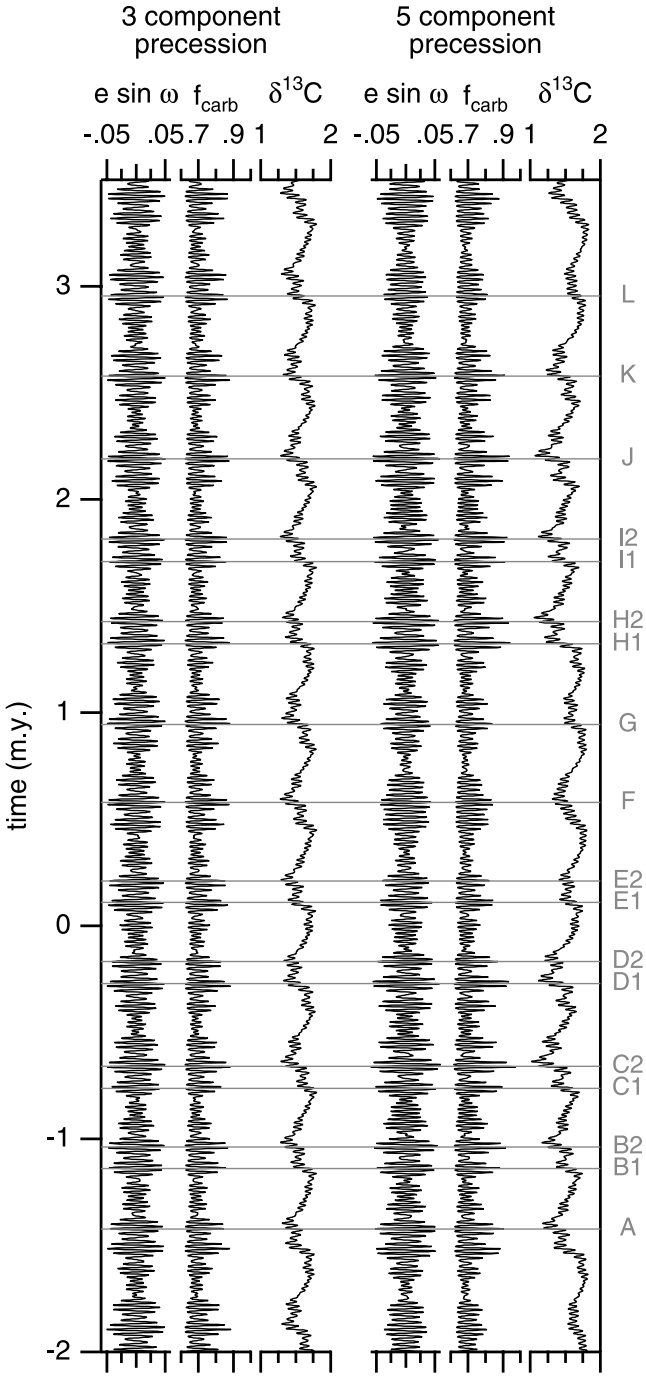

Figure 7. Construction of the $\delta^{13}C$ model. Two instances are shown, using 3 and 5 components for the initial synthetic precession curve. In each case, the three curves correspond (from left to right) to equations (1), (2), and (3) in the text. Lettered horizontal lines mark eccentricity maxima used as tie-points in tuning the actual $\delta^{13}C$ records.

variations are absent. The last assumption is justifiable as long as the oceanic ΣCO_2 and the net flux of carbon from mantle outgassing and weathering were roughly the same as today (i.e., residence time = flux/volume).

[38] The model was implemented mathematically in three steps (Figure 7). First, a synthetic precession curve (representing insolation forcing) was constructed using the equation

$$Prec_t = \sum_{i=1}^{n} A_i \cos\left(\frac{2\pi(t - t_0)}{P_i} + \phi_i\right), \tag{1}$$

where $Prec_t$ is the climatic precession parameter at time t, n is the number of periodic components used, values for A (amplitude), P (period), and ϕ (phase) were taken from *Laskar* [1999], and $t_0 = -6.98$ myr was used to visually match the $\delta^{13}C$ record with the P/E CIE positioned at 0 myr.

[39] Second, a nonlinear transform was applied to represent the carbonate/organic carbon deposition response to insolation forcing using the equation

$$f_{carb_t} = \frac{\text{carbonate carbon deposition}}{\text{carbonate} + \text{organic carbon deposition}} = \exp\left(-\frac{Prec_t + 0.1}{0.04}\right) + 0.6, \tag{2}$$

arbitrarily chosen to vary within realistic bounds. The exponential term in this equation imparts a nonlinearity that must be present to produce cyclicity (rather than simply amplitude modulation) at eccentricity periods. Although this equation is arbitrary, and virtually any nonlinear transformation of the precession curve would serve our purposes as a tuning target, use of a realistic forcing mechanism allows us to make a first-order assessment of the source of the large $\delta^{13}C$ shifts.

[40] Third, the effect of the residence time was incorporated using a recursive function based on a standard $\delta^{13}C$ mass balance equation:

$$\delta^{13}C_t = \delta^{13}C_{t-\Delta t} + \frac{\Delta t}{C_{res}}\delta^{13}C_{in} - \frac{\Delta t}{C_{res}} \cdot \left[f_{carb}\delta^{13}C_{carb} - (1 - f_{carb})\delta^{13}C_{org}\right], \tag{3}$$

where $\delta^{13}C_t$ and $\delta^{13}C_{t\text{-}\Delta t}$ indicate the modeled $\delta^{13}C$ value at the current and previous time steps, $\delta^{13}C_{in} = -5$ was used as the $\delta^{13}C$ value for carbon entering the ocean (from weathering and mantle outgassing), $\delta^{13}C_{org} = \delta^{13}C_{t-\Delta t} - 26$ and $\delta^{13}C_{carb} = \delta^{13}C_{t-\Delta t} + 2$ were used for the $\delta^{13}C$ values of organic carbon and carbonate carbon deposition, and $C_{res} = 0.1$ myr was used to approximate the residence time of carbon [e.g., *Broecker and Peng*, 1982; *Siegenthaler and Sarmiento*, 1993; *Sarmiento and Bender*, 1994].

[41] We recognize that the precession periods used in constructing the synthetic curve are not strictly valid for the early Paleogene [*Berger et al.*, 1992; *Laskar*, 1999], but the timing of the transient spikes is almost entirely controlled by the eccentricity modulation. Since the modulatory periods can be expected to remain constant through geologic time [*Berger et al.*, 1992; *Laskar*, 1999], the exact values used for the precession periods are essentially irrelevant so long as the interaction results in modulation at the correct eccentricity periods.

[42] Modulation occurs as an interference pattern between two sinusoidal curves having similar periods. The modulating period can be calculated as the reciprocal of the difference between the interfering frequencies. In order to obtain the

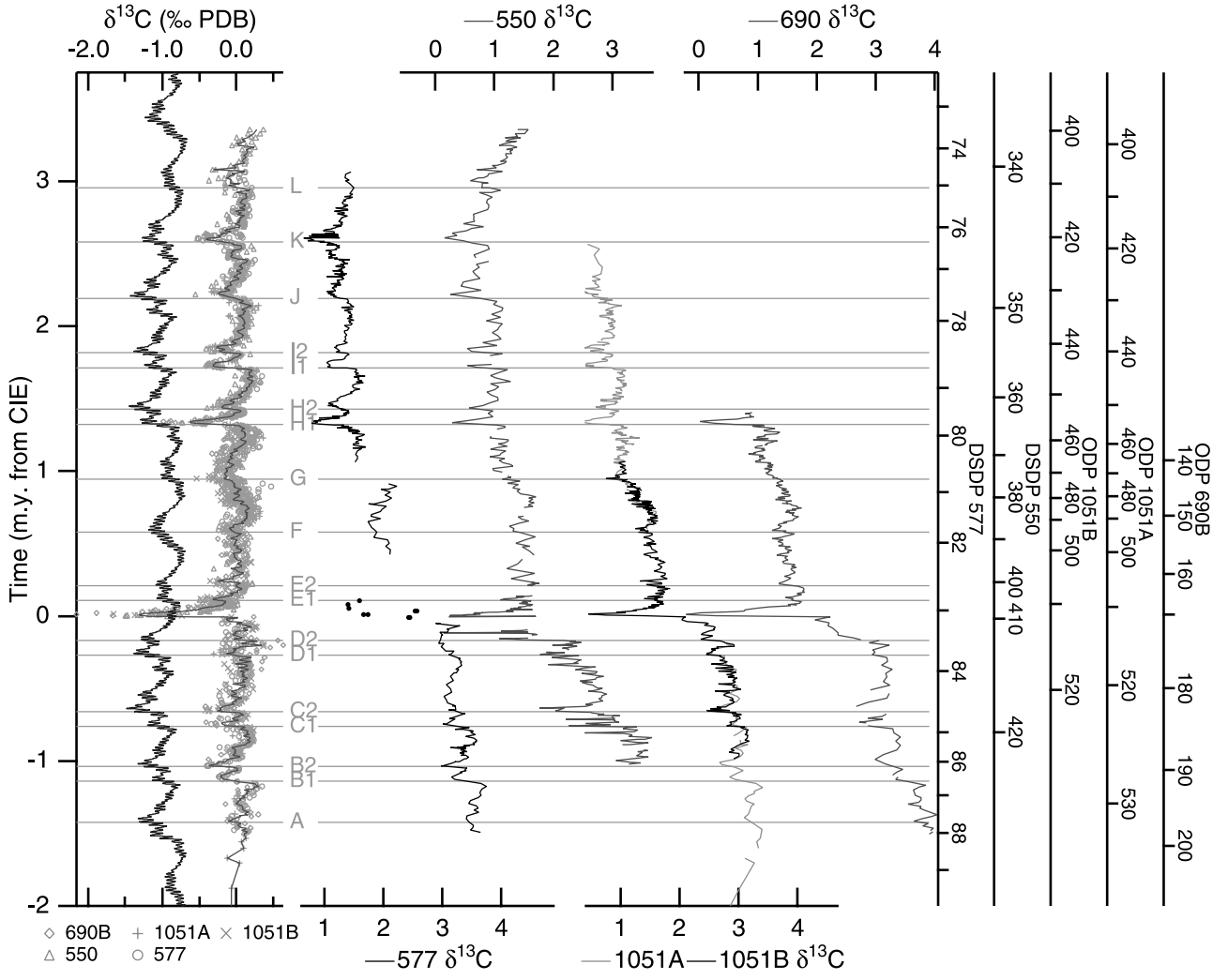

Figure 8. Carbon isotope records for Sites 1051, 690, 550, and 577 plotted against the relative orbital timescale constructed by interpolating between ages assigned to $\delta^{13}C$ transients based on the $\delta^{13}C$ model, shown to the far left. Horizontal lines mark eccentricity maxima and are equivalent to the lettered lines in Figures 3–5. The modeled $\delta^{13}C$ record is plotted on the same scale with a stacked and smoothed (using a gaussian filter with a 10% response at 1.67 cycles/myr) $\delta^{13}C$ record combining data from all four sites; data from Site 550 below the CIE were not included in the stack (see text for explanation). See color version of this figure in the HTML.

dominant periods of the short (~95 and ~124 kyr) and long (~405 kyr) eccentricity components, it is only necessary to use the first three periodic components of precession. However, the addition of the fourth and fifth periodic components adds longer modulating frequencies of ~1.0 and ~2.4 myr (several others simply add to the power in the short eccentricity band) which are of interest to us: they explain the interval of low amplitude variations in the $\delta^{13}C$ records just above the CIE (Figures 7 and 8). It should be noted that the uncertainty in the period of the very long eccentricity (~2.4 myr ±25%) cycle is substantially larger than for the other eccentricity periods (±2% for the several components at ~100 kyr and ±0.4% for the ~400 kyr component) because it involves only unstable fundamental frequencies of the solar system (g3 and g4, as opposed to the more stable g5 and g2 terms) [*Laskar*, 1990, 1999; *Olsen and Kent*, 1999].

[43] The resulting target curve bears a strong resemblance to the measured $\delta^{13}C$ records, with transient decreases occurring at high-amplitude intervals (controlled by maxima in eccentricity) in the precession curve (Figures 7 and 8). We note that times of most rapidly decreasing $\delta^{13}C$ values correspond with peaks in the precession amplitude and therefore with maxima in eccentricity. Most of the transient decreases occur in pairs, reflecting the presence of two short eccentricity maxima within the high-amplitude portion of the long eccentricity modulation.

3.4. Eccentricity-Based Tuning

[44] To accomplish the actual tuning, we chose the simplest method of using each transient decrease in the $\delta^{13}C$ data as an age calibration tie-point and applying a linear interpolation between transients (Figures 8 and 9,

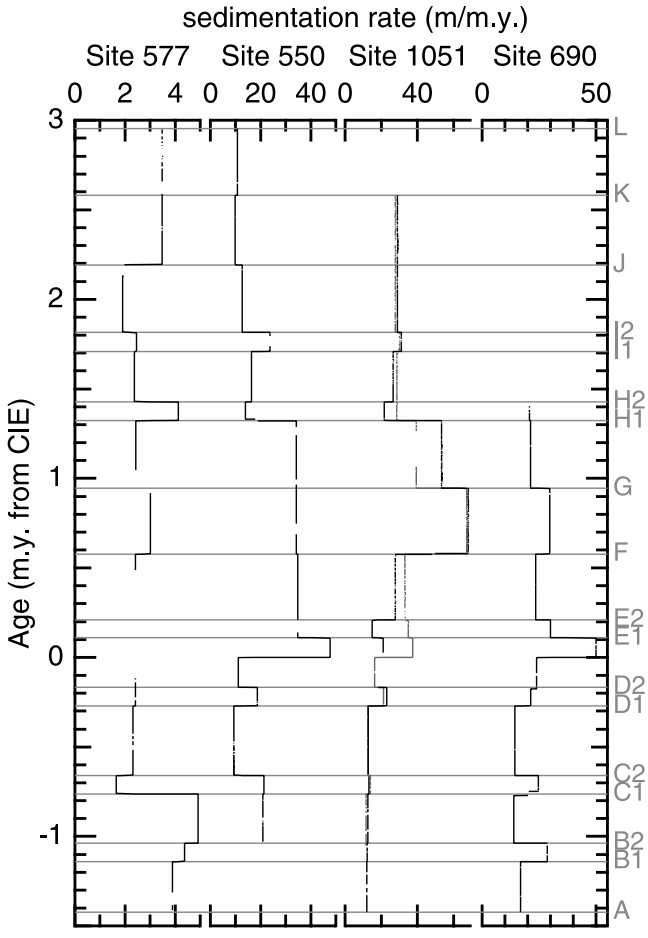

Figure 9. Sedimentation rates implied by the orbital age calibration. For Site 1051, the black line represents Hole 1051A and the gray line represents Hole 1051B. Gaps reflect data gaps due to lack of recovery.

Table 1). While it might seem preferable to use a more typical tuning algorithm that seeks to maximize the total covariance between the data and target curve [e.g., *Martinson et al.*, 1982], such a method would imply a level of confidence in the details of our model that we do not believe is justified. We could also have used a spline interpolation between transient decreases, resulting in more aesthetically pleasing smooth sedimentation rate variations, but it is not obvious that this would be more accurate. It is likely that sedimentation rates varied cyclically in response to Milankovitch forcing, and an accurate reconstruction of this cyclicity would require additional control points.

[45] In an initial tuning step, we used only eccentricity maxima A–C and H–L, excluding the interval surrounding the CIE as well as the interval of low amplitude variations above the CIE and correlating eccentricity maximum H with the first large decrease above the low amplitude interval in the tuning target. Recognizing that one of our objectives was to test whether the CIE may have occurred at an eccentricity maximum, we relied heavily on precessional cyclicity in color and magnetic susceptibility logs from Sites 690 and 1051 in order to identify tuning tie-points surrounding the CIE. At both sites, the $\delta^{13}C$ decrease we label D1 occurs 15–18 lithologic cycles (~0.33 myr) above eccentricity maximum C2 (Figure 10). This is consistent both with the expected temporal separation between these two eccentricity maxima in our tuning target and with the number of lithologic cycles observed between transients B2 and C1 (confirming that the lithologic cyclicity is consistent through the records). The interval above transient D1 is compromised at Site 1051 by the presence of a laminated unit with a distinctly different character from the underlying bioturbated sediments, which display smoothly varying lithologic cyclicity (Figure 10). We therefore relied only on Site 690 to confirm that the $\delta^{13}C$ decrease we label D2 occurs 5–6 lithologic cycles above transient D1. This is again consistent with the number of cycles observed between other paired transients as well as the predicted temporal separation in our tuning target.

[46] The CIE is separated by only 7–9 cycles (~0.17 myr) from transient D2 at both sites (Figure 10), indicating either that the CIE cannot be correlative with the subsequent eccentricity maximum or that this interval is temporally discontinuous at Sites 1051 and 690. Although the lithologic cyclicity is less clear in the interval immediately above the CIE, there is a significant $\delta^{13}C$ decrease (E2) that occurs 14–25 cycles (~0.40 myr) above transient D2, with a more subtle decrease (E1) 11–20 cycles above transient D2 (Figure 10). Although they do not provide definitive confirmation, these cycle counts are consistent with our conclusion that the timing of the CIE is anomalous in the context of eccentricity-controlled $\delta^{13}C$ decreases.

[47] Since the low amplitude of $\delta^{13}C$ variations above the CIE can be explained as the result of modulation by the very long eccentricity (~2.4 myr) cycle, in our final tuning we used $\delta^{13}C$ decreases as tie-points for eccentricity maxima F

Table 1. Depths and Relative Ages of Eccentricity Maxima[a]

		Depth, mbsf				
Event	Age	690	1051A	1051B	550	577
L	2.95	—	—	—	341.56	—
K	2.58	—	—	—	345.58	76.35
J	2.19	—	429.64	431.52	349.17	77.70
I2	1.82	—	440.26	441.74	353.97	78.42
I1	1.71	—	443.55	444.93	356.71	78.68
H2	1.43	—	450.78	452.89	361.30	79.32
690 hiatus[b]	1.40	133.19	—	—	—	—
H1	1.32	134.90	453.02	455.84	362.74	79.75
G	0.94	142.76	472.06	471.67	379.56	80.73
F	0.58	153.44	496.24	495.85	397.39	81.83
E2	0.21	161.92	507.59	507.66	404.60	—
E1	0.11	164.92	509.08	509.00	407.54	—
CIE	0.00	170.63	511.37	512.91	409.79	—
D2	−0.17	174.56	514.93	515.64	411.64	—
D1	−0.27	176.78	517.33	517.04	413.46	83.75
C2	−0.66	182.32	522.32	521.89	417.07	84.65
C1	−0.76	185.51	523.69	523.33	419.24	84.82
550 hiatus[b]	−1.03	—	—	—	425.00	—
B2	−1.04	189.33	526.91	526.58	—	86.17
B1	−1.14	192.33	528.16	—	—	86.62
A	−1.42	197.22	531.56	—	—	87.72

[a]Orbitally tuned chronologies were constructed by linear interpolation between these datums.

[b]Unconformities at Sites 550 and 690 are included because they were used as tie-points at these sites; ages for these unconformities were obtained by linear interpolation from the nearest carbon isotope transient decreases.

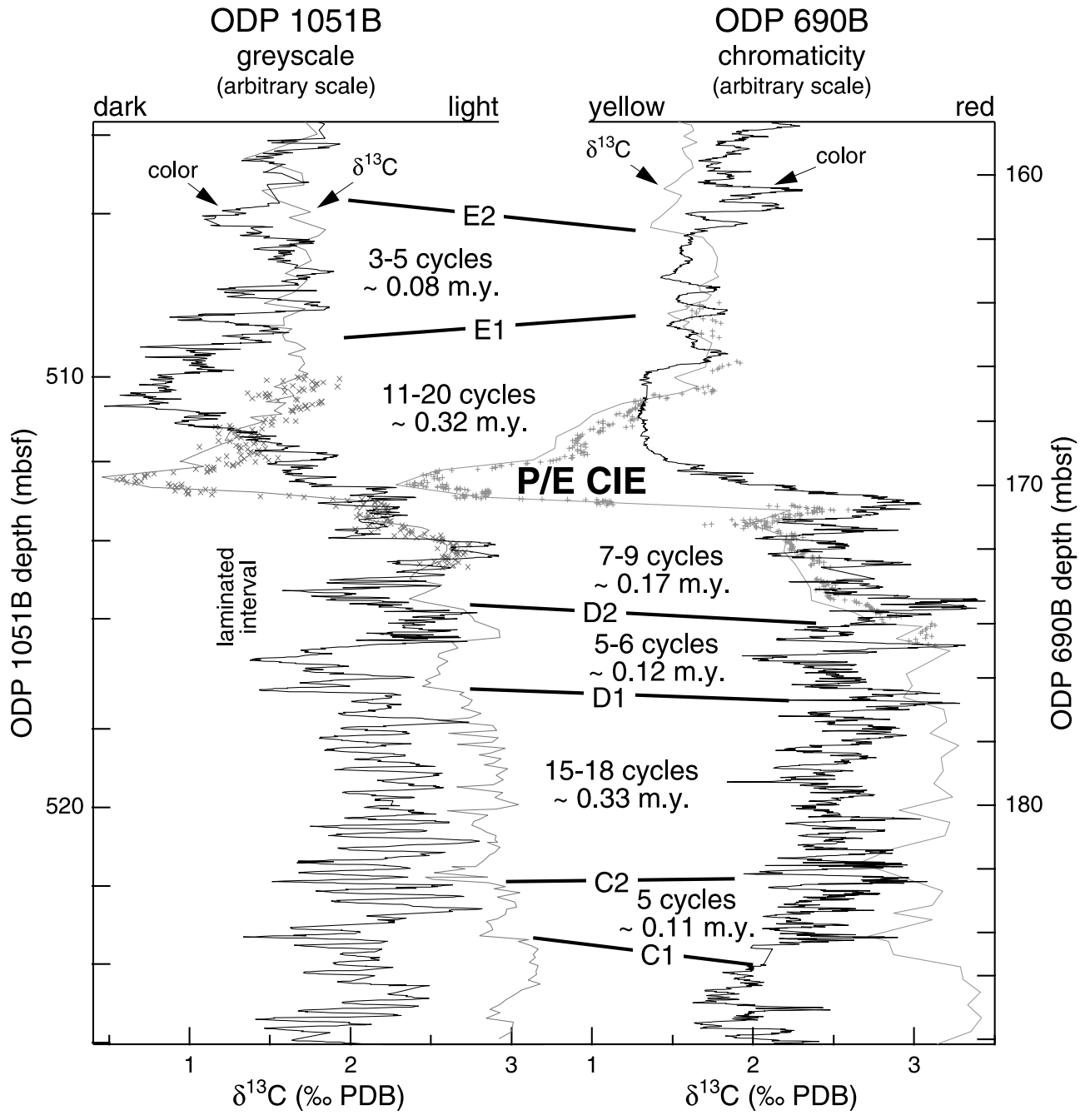

Figure 10. Sediment color logs and carbon isotope records from Holes 690B and 1051B for a ~1.5 myr interval including the CIE. Lines between the two records demarcate the $\delta^{13}C$ transients; cycle counts in the logs constrain the duration between these transients. The different character of the Site 1051 log in the interval from ~514.5 to ~517 mbsf is due to a change in lithology from bioturbated sediments below to laminated/bedded sediments within this interval, which we interpret as having been deposited rapidly. High-resolution data points through the CIE are from *Bains et al.* [1999]. The records are plotted relative to total core recovery, but depth labels have been adjusted to correspond to ODP standard mbsf. Spacing between tick marks on the depth axis is uneven due to excess recovery and voids. See color version of this figure in the HTML.

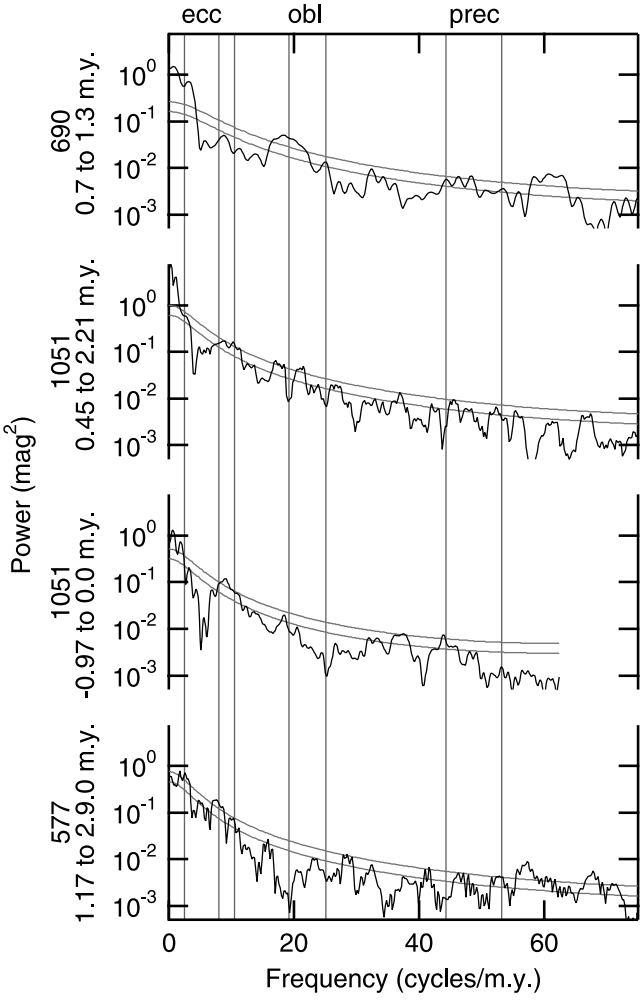

Figure 11. Multitaper spectral analysis of high-resolution intervals in tuned $\delta^{13}C$ records. Vertical lines correspond to the principal frequencies for eccentricity, obliquity, and precession. Carbon isotope records were detrended using a gaussian filter with cutoff (10% response) at a frequency of 0.5 cycles/myr and then interpolated to a constant sampling interval of 4 kyr for Site 690 and the younger segment from Site 1051, 5 kyr for Site 577, and 8 kyr for the older segment from Site 1051. The records from Holes 1051A and 1051B were spliced together to create a continuous record through the interval. Multitaper spectral analysis was performed using the SSA-MTM Toolkit [*Ghil et al.*, 2002] with robust red-noise significance testing; smooth gray lines indicate 0.90 and 0.99 confidence levels for each spectrum.

and G (see Figure 4). We must acknowledge that the uncertainty in our final tuning is greater in this interval than in intervals with larger amplitude $\delta^{13}C$ variations. We also used the CIE as an additional tie-point, assigning an age of 0.170 myr (~8 precession cycles) younger than the preceding eccentricity transient, in order to ensure that it is correlative in the orbitally tuned records. This results in a significant increase in sedimentation rates in the recovery interval of the CIE at Sites 690 and 550. Our calibration for Site 690 is not consistent in this respect with that of *Röhl et al.* [2000], which was based on lithologic cyclicity of presumed precessional origin, but instead reinforces sedimentation rate estimates based on ^{3}He abundances [*Farley and Eltgroth*, 2003].

3.5. Testing the Tuning

[48] Several intervals of the $\delta^{13}C$ records are sampled at sufficiently high resolution that precessional cyclicity should be observed. We have noted that there is cyclicity present in the isotopic records that correlates with cyclicity in geophysical logs, which has been presumed to be precessional in origin [*Norris and Röhl*, 1999; *Röhl et al.*, 2000; *Cramer*, 2001]. We computed spectra for high-resolution intervals of the $\delta^{13}C$ records using a multitaper method (SSA-MTM Toolkit [*Ghil et al.*, 2002]). The spectra show significant power at the frequencies of short (~10.5 and ~8 cycles/myr) and long (~2.5 cycles/myr) eccentricity, as expected since these were the components used in tuning the records (Figure 11; the lack of significant peaks at short-eccentricity frequencies in the spectrum for Site 690 reflects the position of this data segment in the interval of low eccentricity amplitude while the lack of a significant peak at the long-eccentricity frequency for the pre-CIE segment from Site 1051 results from the short length of that segment, capturing only two 400-kyr cycles). The records show statistically significant power in the precession band (~45–50 cycles/myr); a statistical test indicates that there is a $\ll$1% chance that this power reflects a random process. The tuning process could not have focused power in this frequency band because the age-calibration tie-points used are separated by at least ~100 kyr. The spectra therefore strongly support a precession control on high-frequency variability in the carbon cycle. There is also power in the obliquity band (~24 cycles/myr) at Sites 690 and 1051, perhaps indicating that high-latitude processes had some effect on the carbon cycle during this time period.

[49] The geophysical logs provide a better means of testing our tuning since they are sampled at sufficiently high resolution to observe precessional cyclicity throughout. We calculated spectra for the tuned sediment logs using the multitaper method as well as wavelet transforms (Figure 12; wavelet analysis available in an appendix file in the online auxiliary material[1]). The spectra show significant power in the eccentricity band for all sites, with significant precession power at Sites 690 and 1051 and significant obliquity power at Site 550. Although it has been suggested that obliquity is represented in the lithologic cyclicity at Site 690 [*Cramer*, 2001], peaks in the obliquity band for this site are only marginally significant. The low amplitude of peaks in the precession band for Site 577 likely reflects both a dampening of power at high frequencies due to bioturbation in a low-sedimentation environment (10 kyr is represented by only ~2 cm in the core) and a greater relative variability in sedimentation rates which is not fully captured with our age model.

[50] A more realistic view of the effects of our tuning is provided by wavelet analyses (available in an appendix file in the online auxiliary material[1]), which show considerable variability in the period associated with precession and obliquity cycles. This variability can be attributed to the wide spacing of the tie-points used for tuning relative to

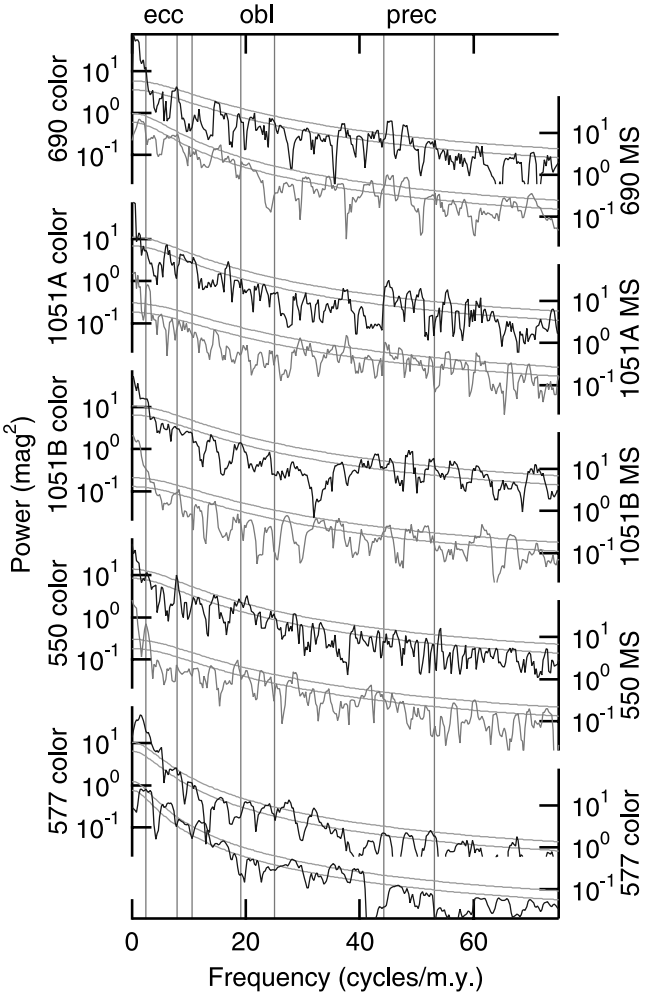

Figure 12. Multitaper spectral analysis of tuned sediment color and magnetic susceptibility logs. Vertical lines correspond to the principal frequencies of eccentricity, obliquity, and precession. Logs were interpolated to a constant sampling interval of 4 kyr and normalized to unit variance. Multitaper spectral analysis was performed using the SSA-MTM Toolkit [*Ghil et al.*, 2002] with robust red-noise significance testing; smooth gray lines indicate 0.90 and 0.99 confidence levels for each spectrum. For Holes 690B, 1051A, 1051B, and 550 the spectrum for sediment color is shown in blue (dark) while that for magnetic susceptibility (MS) is shown in red (light). No magnetic susceptibility log was available for Site 577. To avoid the discontinuous interval in the middle of the site 577 Section, the record was analyzed in two segments: the spectrum for 1.2 to 3.0 myr is shown above while that for −1.4 to −0.1 myr is shown below. See color version of this figure in the HTML.

precession and obliquity periods and is therefore a measure of the accuracy of our tuning on subeccentricity timescales. The wavelet analyses also demonstrate a distinct modulation of the precession amplitude at Sites 690 and 1051 by both the ∼0.1 and ∼0.4 myr eccentricity components, confirming that the δ^{13}C transient decreases occur at maxima in the precession amplitude.

3.6. Error Analysis

[51] The error in the orbital tuning can be attributed to the error in the tuning target used and the error in matching the δ^{13}C records. The error in the tuning target is trivial: we use the tuning only to establish a relative timescale based on known eccentricity periods, which should be correct within ∼1% [e.g., *Berger et al.*, 1992], or ≪0.01 myr; the error in the phase is substantially greater for the early Paleogene and prohibits using the tuning target to obtain an accurate numerical age. The error in matching the δ^{13}C records to the target results primarily from our use of linear interpolation between δ^{13}C transients. We suspect that actual sedimentation rates vary in response to orbital forcing of climate and should therefore be cyclic. In this case, the linear interpolation used will be close to the mean sedimentation rate over the period of the dominant cycle, and the age model at any point should not be in error by more than some fraction of that period. If sedimentation rates vary with eccentricity, then the pertinent cycle would likely be that of short eccentricity (∼0.1 myr). We therefore suggest that an error estimate of ±0.03 myr is appropriate, or ∼2/3 of a short eccentricity period.

[52] Use of the carbon isotope records allows construction of an orbital chronology accurate at the long-eccentricity (∼0.4 myr) and, to a slightly lesser degree, short eccentricity (∼0.1 myr) scale. In detail, the wavelet analyses show the shortcomings of the linear interpolation used in our tuning. For instance, in Hole 1051B at eccentricity maximum G there are three high amplitude regions that clearly reflect eccentricity modulation of precessional cyclicity, but two of the three fall outside of the precessional band in our tuning. Such features could be used for high-precision calibration of specific events in sections with well-developed lithologic cyclicity. We have not taken further steps to refine the stratigraphies presented here, instead concentrating on the development of an orbital stratigraphic framework that can be easily used for eccentricity-scale correlation among sites. Similarly, a rigorous analysis of the error in our tuning is not appropriate because that error can be substantially reduced when necessary for specific purposes.

3.7. Integration of Magnetostratigraphy and Biostratigraphy

[53] The correlation of magnetic polarity reversals among the four sites relative to the eccentricity timescale is generally excellent (Figure 13, Table 2). The base of chron C25n occurs just below maximum B at Sites 577, 690, and 1051; it is not present at Site 550 due to a hiatus. The C24r/C25n reversal is located between eccentricity maxima B and C at all four sites. The C24n/C24r reversal occurs in the lower portion of the interval between eccentricity maxima H and I at Sites 550 and 1051 while the C24n.2r/C24n.3n reversal occurs immediately below eccentricity maximum J at these sites. These reversals are not present at Site 690 due to a hiatus. Both reversals are slightly lower at Site 577, but the discrepancy is actually due only to a single sample in each case and may result from a combination of low and highly variable sedimentation rates (Figure 9) and poor core preservation. We also emphasize that the quality of the magnetostratigraphic record in this interval is often quite poor, especially in the upper part of chron C24r, which may reflect a time period of

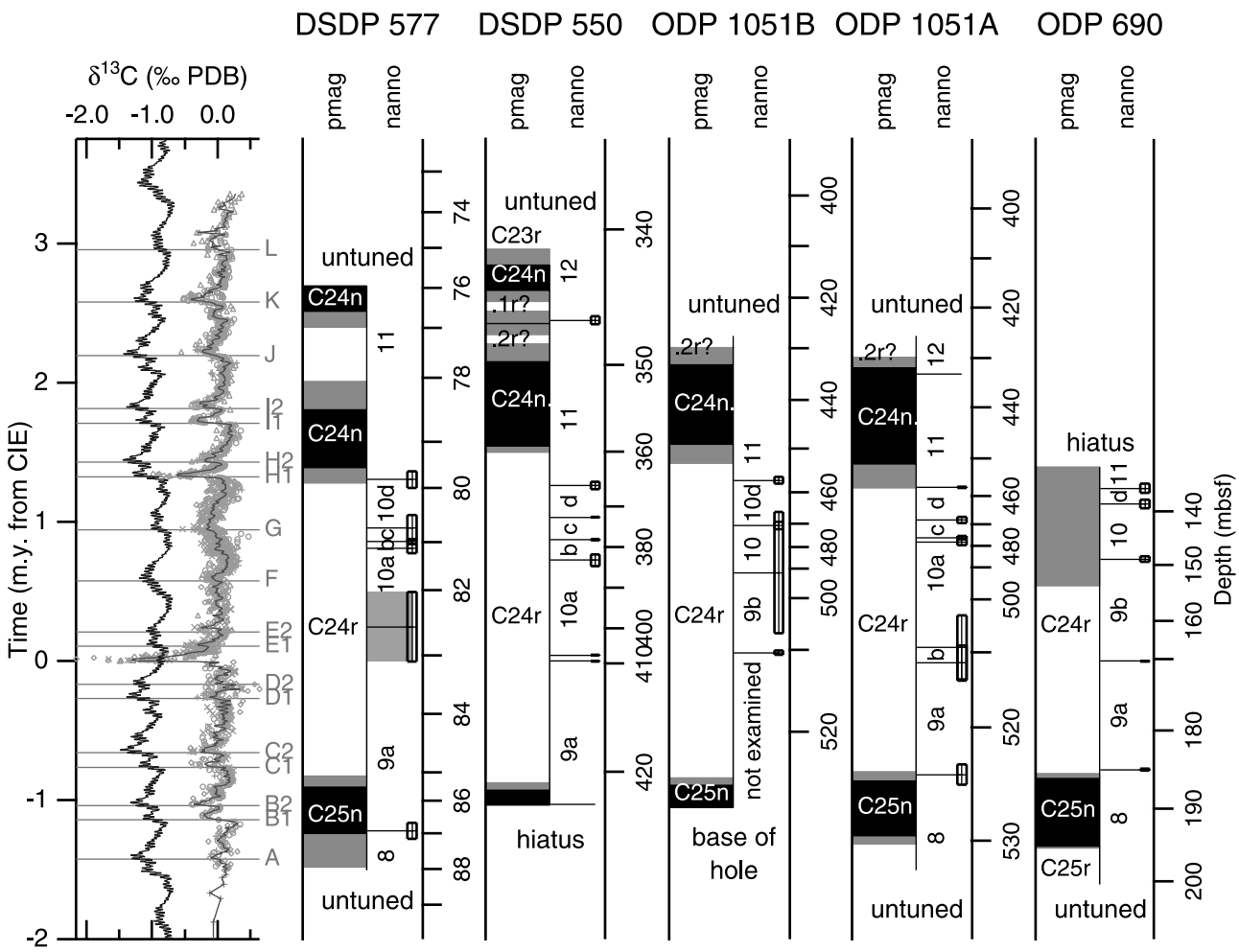

Figure 13. Stacked carbon isotope record, magnetic polarity zonations, and nannofossil biostratigraphic zonations for Sites 1051, 690, 550 and 577 plotted relative to the orbitally calibrated timescale. Boxes at the ends of lines marking nannofossil (sub)zonal boundaries and gray areas at magnetic polarity transitions indicate the uncertainty due to sampling resolution and nondiagnostic data; the error associated with the orbital tuning is not added. See color version of this figure in the HTML.

Table 2. Depths and Calibrated Relative Ages for Magnetic Polarity Zonal Boundaries

Chron, base	690 mbsf	1051A mbsf	1051B mbsf	550 mbsf	577 mbsf	
C23r	—	—	—	342.07 ± 0.61	—	
C24n.1n	—	—	—	345.07 ± 0.45	76.77 ± 0.20	
C24n.1r	—	—	—	346.50 ± 0.34	—	
C24n.2n	—	427.75 ± 2.10	428.59 ± 1.10	347.23 ± 0.39	—	
C24n.2r	—	430.89 ± 1.04	431.43 ± 1.74	348.97 ± 0.71	78.24 ± 0.20	
C24n.3n	—	453.90 ± 2.95	450.94 ± 1.96	359.68 ± 0.34	79.68 ± 0.20	
C24r	186.31 ± 0.25	524.34 ± 0.29	524.49 ± 0.30	422.12 ± 0.61	85.32 ± 0.20	
C25n	195.69 ± 0.13	529.86 ± 0.35	—	425.09 ± 0.08	87.46 ± 0.47	
Chron, base	690 Age[a]	1051A Age[a]	1051B Age[a]	550 Age[a]	577 Age[a]	BKSA age[b]
C23r	—	—	—	2.91 ± 0.06	—	2.64
C24n.1n	—	—	—	2.63 ± 0.04	2.46 ± 0.06	2.34
C24n.1r	—	—	—	2.48 ± 0.05	—	2.24
C24n.2n	—	2.26 ± 0.08	2.30 ± 0.04	2.39 ± 0.04	—	2.20
C24n.2r	—	2.15 ± 0.04	2.20 ± 0.06	2.22 ± 0.07	1.91 ± 0.10	2.10
C24n.3n	—	1.34 ± 0.08	1.50 ± 0.07	1.53 ± 0.02	1.34 ± 0.06	1.65
C24r	−0.82 ± 0.02	−0.82 ± 0.03	−0.86 ± 0.03	−0.90 ± 0.03	−0.86 ± 0.04	−0.90
C25n	−1.33 ± 0.01	−1.28 ± 0.03	—	—	−1.36 ± 0.12	−1.39

[a]Errors take into account only the distance between interpreted samples; the error associated with the orbital tuning is not added.
[b]Relative ages according to the timescale of *Berggren et al.* [1995], calculated by subtracting their ages from 55, are shown for comparison.

Table 3. Depths and Calibrated Relative Ages for Nannofossil Zonal Boundaries

Zone, base	690 mbsf	1051A mbsf	1051B mbsf	550 mbsf	577 mbsf	
NP12	—	433.40 ± —	—	346.77 ± 0.19	—	
NP11	136.65 ± 0.75	457.01 ± 0.29	456.69 ± 0.93	364.85 ± 0.85	79.83 ± 0.16	
NP10d	138.90 ± 0.68	468.34 ± 1.10	470.52 ± 1.05	372.70 ± 0.07	80.68 ± 0.25	
NP10c	—	475.90 ± 0.75	—	378.23 ± 0.17	80.99 ± 0.06	
NP10b	—	478.05 ± 1.40	—	383.28 ± 1.40	81.14 ± 0.10	
NP10a	148.88 ± 0.52	510.65 ± 4.80	490.91 ± 19.34	407.80 ± 0.05	82.57 ± 0.53	
NP9b	170.63 ± 0.00	512.77 ± 2.69	510.77 ± 0.51	409.79 ± 0.00	—	
NP9a	185.79 ± 0.09	524.26 ± 0.82	—	—	86.93 ± 0.22	
Zone, base	690 Age[a]	1051A Age[a]	1051B Age[a]	550 Age[a]	577 Age[a]	BKSA age[b]
NP12	—	2.06 ± —	—	2.45 ± 0.03	—	2.15
NP11	1.24 ± 0.04	1.25 ± 0.01	1.30 ± 0.03	1.26 ± 0.02	1.30 ± 0.06	1.39
NP10d	1.13 ± 0.03	1.01 ± 0.02	0.97 ± 0.03	1.03 ± 0.00	0.96 ± 0.09	1.07
NP10c	—	0.89 ± 0.01	—	0.87 ± 0.00	0.86 ± 0.02	0.83
NP10b	—	0.85 ± 0.02	—	0.72 ± 0.04	0.81 ± 0.03	0.63
NP10a	0.73 ± 0.02	0.10 ± 0.23	0.64 ± 0.44	0.04 ± 0.00	0.25 ± 0.25	0.00
NP9b	0.00 ± 0.00	−0.01 ± 0.13	0.06 ± 0.02	0.00 ± 0.00	—	−0.50
NP9a	−0.78 ± 0.01	−0.82 ± 0.07	—	−1.03 ± —	−1.22 ± 0.06	−1.20

[a]Errors take into account only the distance between interpreted samples; the error associated with the orbital tuning is not added.
[b]Relative ages according to the timescale of *Berggren et al.* [1995], modified following *Aubry et al*. [1996], *Aubry* [1996], and *Aubry and Sanfilippo* [1999], calculated by subtracting their ages from 55, are shown for comparison.

low field intensity [*Cande and Kent*, 1992b; *Gee and Cande*, 2002]. The boundaries of subchron C24n.1n correlate well between Sites 550 and 577, although this interval was outside the primary focus of our tuning efforts; we did not generate carbon isotope records through the equivalent section at Site 1051. In general, the combined error due to sampling interval and tuning in the calibrated age of each reversal at each site is greater than the mismatch between sites.

[54] The correlation of the biostratigraphic boundaries in the NP9-NP10 zonal interval with regard to the eccentricity timescale is also generally excellent, although there are striking inconsistencies. The NP10d/NP11 zonal boundary (highest occurrence [HO] of *Tribrachiatus contortus*) lies slightly below eccentricity maximum H1 at Sites 1051B, 550, 577 and 690. The base of Subzone NP10d (lowest occurrence [LO] of *T. contortus*) lies slightly above transient G and is essentially of the same age at Sites 1051A, 550 and 577, and the base of Subzone NP10c (HO *T. digitalis*) is essentially correlative as well (Figure 13, Table 3). The calibrated age for the base of Subzone NP10b (LO *T. digitalis*) is slightly older at Site 550 than at Sites 1051A and 577, but this is likely due to our inability to identify $\delta^{13}C$ transient G at Site 550 (due to the coring gap between Cores 30 and 31, 374–375 mbsf; Figure 4). Whereas most of the zonal boundaries correlate well within the combined error (~100 kyr) of sampling interval and tuning there are two remarkable differences, which seem to imply diachrony of the NP8/NP9 and NP9/NP10 zonal boundaries. The base of Zone NP9 (LO of *Discoaster multiradiatus*) would appear to be 0.3 myr younger at Sites 690 and 1051A (close to transient C1) than at Site 577 (below transient B). The base of Zone NP10 (LO of *T. bramlettei*) would appear to be 0.6 myr younger at high southern latitude Site 690 (between eccentricity transients F and G) than elsewhere (between transients E and F). This seeming diachrony is weakened, however, if one takes into account reported uncertainties in the delineation of these boundaries. Whereas the NP8/NP9 zonal boundary is clearly delineated at Site 577 [*Monechi*, 1985; *Aubry et al.*, 1996], *Aubry et al.* [1996] cautioned that its delineation in Hole 690 was not firm because of the extreme scarcity of discoasters at 185.70 mbsf and below. The problem is very different regarding the base of Zone NP10 at Site 690. For a multitude of reasons (involving taxonomy, preservation, ecology), the delineation of the base of Zone NP10 has long been contentious [*Aubry et al.*, 2000]. *Aubry et al.* [1996] observed that *T. bramlettei* is exceedingly rare between 150.94 and 148.40 mbsf at Site 690. In poorly preserved sediments, as at Site 690, *T. bramlettei* is difficult to differentiate from *Rhomboaster cuspis*. It is thus likely that the base of NP10 at Site 690 was taken at the level of lowest common occurrence of *T. bramlettei* [*Pospichal and Wise*, 1990; *Aubry et al.*, 1996]. Future work must be done with the guidance of cyclostratigraphy to determine the true temporal/geographic distribution of *D. multiradiatus* and *T. bramlettei*.

3.8. Temporal Representation

[55] The cycles are easily correlated among the four sections and the correlation is reinforced by the similarity of long-term (>1 myr) trends in isotope values (Figure 8). We recognize only two hiatuses in the sections studied, each of which is clearly identifiable in the carbon isotope records as well as being implied by magnetostratigraphic and biostratigraphic correlations:

[56] 1. At Site 690, a hiatus occurs between 133.26 and 133.11 mbsf (samples 15-4, 51 cm and 15-4, 66 cm). There is not a prominent lithologic change at this level, although the thickness of (precessional) lithologic cycles decreases substantially. The hiatus is obvious from the carbon isotope record as an abrupt 0.8‰ increase where correlation with the other three sites indicates that values should decrease if the section were continuous. Nannofossil biostratigraphy suggests that there may be several hiatuses in this interval, based on the close juxtaposition of the NP10/NP11, NP11/NP12, and NP12/NP14 zonal contacts [*Berggren and Aubry*, 1996; *Aubry et al.*, 1996] (Figure 3).

[57] 2. At Site 550, a hiatus occurs at ~425 mbsf and is marked by a thick manganese-rich bed that is unmistakable in the core [see *Ali and Hailwood*, 1998]. Carbon isotope

values decrease by >1.5‰ through this interval, and the absence of nannofossil Zones NP6-NP8 confirms that the interval is unconformable (Figure 5).

[58] The difference in lithologic expression between these two hiatuses likely reflects a difference in mechanism: the hiatus at Site 550 appears to represent a period of sediment starvation resulting in a thick manganese-rich condensed interval while the lack of a lithologic expression at Site 690 suggests instead an erosional mechanism and no slow sedimentation.

[59] *Cramer* [2001] suggested that a hiatus was present at Site 690 between the CIE and the base of NP9 based on a discrepancy between the number of presumed precession cycles counted at Sites 690 and 1051. Since the eccentricity tuning indicates that the NP8/NP9 contact is correlative between Sites 1051 and 690, the discrepancy in cycle counts must still be explained. We note that the level of the NP8/NP9 contact at Site 690 occurs at ~185.8 mbsf, in the upper portion of core 22, section 1 which shows severe drilling disturbance. The section above (core 21 section 4) is also disturbed due to a collapsed liner. We therefore prefer at this time to interpret the shortage of lithologic cycles at Site 690 as due to lack of recovery rather than a hiatus in sedimentation.

4. Discussion

4.1. Implications for Chronostratigraphy

[60] The method used to construct the chronology presented here is robust because it combines the cyclostratigraphic and chemostratigraphic advantages of $\delta^{13}C$ records. Carbon isotope records have been used as a correlation tool in previous studies of the latest Paleocene–earliest Eocene [*Stott et al.*, 1996; *Shackleton et al.*, 1985] but only from an empirical standpoint: similarities in carbon isotope records were assumed to correlate due to the two-order-of-magnitude difference between the ocean mixing time (10^3 yr) and the residence time of carbon (10^5 yr). Placing the variations in $\delta^{13}C$ within a Milankovitch framework adds a predictable element that is lacking for most correlation tools: there is a temporal implication to the identification of carbon isotope events. The use of $\delta^{13}C$ records is also an improvement over most other cyclostratigraphic proxies, which are of little use in site-to-site correlation. It is similar to the now ubiquitous use of oxygen isotope records in the Pleistocene, which reflect a broad spectrum of Milankovitch frequencies.

4.1.1. Magnetochronology and Nannofossil Biochronology

[61] Our orbitally tuned chronology indicates an age of ~1.3 myr older than the CIE for the base of chron C25n, ~0.85 myr older than the CIE for the base of chron C24r, ~1.5 myr younger than the CIE for the base of chron C24n.3n, and ~2.2 myr younger than the CIE for the base of chron 24n.2r (Table 2). The calibrated durations of magnetic polarity chrons C25n, C24r, and C24n.3n are therefore ~0.45, ~2.35, and ~0.7 myr, respectively. *Cande and Kent* [1992a, 1995] gave durations for C25n and C24r of 0.487 and 2.55 myr, consistent with our orbital calibration (the error in our calibration is approximately ±0.1 myr for each reversal, while *Cande and Kent* [1992a] cite an error for the width of Anomalies 24 and 25 of 9.4 and 9.7%, respectively). We also note that the orbitally calibrated

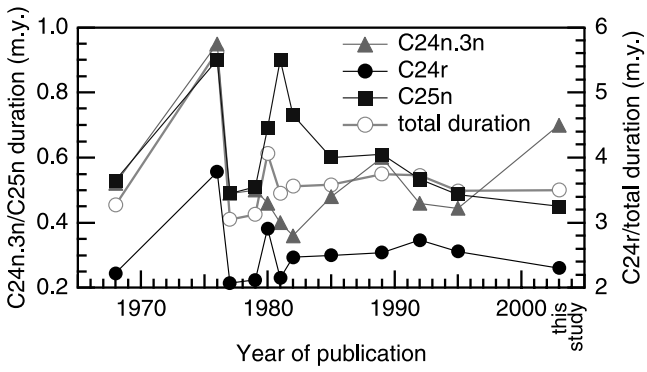

Figure 14. Comparison of estimated durations for magnetic polarity zones according to year of publication (data taken from *Mead* [1996]). See color version of this figure in the HTML.

durations of these two chrons are within the range of previous estimates (Figure 14; *Mead* [1996]) and that the duration of C25n is consistent with cycle counts made at Site 1051 [*Norris and Röhl*, 1999] and Zumaia, Spain [*Dinarès-Turell et al.*, 2002].

[62] The duration for C24n.3n (58% longer than the 0.444 myr duration estimated by *Cande and Kent* [1995]; Table 2) is more troublesome. While the timescale of *Cande and Kent* [1992a, 1995] is based on a seafloor spreading history tied to a calibration point within anomaly 24 that may have been poorly chosen [e.g., *Aubry*, 1998], our orbital calibration demonstrates that the position of that tie-point (55 Ma for a position 2/3 down in anomaly 24) is, perhaps fortuitously, quite accurate. We note that the spline interpolation used to construct the seafloor spreading history [*Cande and Kent*, 1992a, 1995] is quite robust and only a very substantial error in the positioning of a tie-point could account for the difference with our orbital calibration. Our calibrated duration is also longer than that of any previous author with the exception of the anomalous calibration by *Tarling and Mitchell* [1976] (Figure 14). There are two possible explanations for the orbitally derived duration for C24n.3n: either (1) there was an anomalously rapid increase in spreading rates in the South Atlantic during this time or (2) the magnetic polarity records for the sites presented here are compromised in some fashion. In support of the latter possibility, the total duration of chrons C24n.3n–C25n in our calibration is the same as that of *Cande and Kent* [1995], suggesting that there may be a problem with the placement of the C24n/C24r boundary. However, our orbital calibration for Site 550 suggests that the late part of chron C24n may also be longer than estimated by *Cande and Kent* [1995] (Table 2), which would be consistent with an increase in spreading rates.

[63] We have demonstrated that most nannofossil (sub)-biozonal boundaries are essentially synchronous globally. At the same time, we have determined that the NP8/NP9 (LO *D. multiradiatus*) and NP9/NP10 (LO *T. bramlettei*) zonal boundaries may be diachronous; these two problematic zonal boundaries are of great significance, one (NP8/NP9) because it has been considered among the most reliable of Paleogene biostratigraphy (see discussion of *Berggren et al.*

[1995]), the other (NP9/NP10) because it has often been equated with the Paleocene/Eocene boundary [see *Berggren and Aubry*, 1996]. However, we have reasons to suspect that this diachrony is only apparent, and quantitative work is now in progress to resolve this problem. The development of Neogene cyclostratigraphy has resulted in considerable improvements in biostratigraphy by providing a framework with which to test routinely the reliability of paleontologic datums. Likewise, the cyclostratigraphic framework established here will provide guidance to test the reliability of late Paleocene–early Eocene biostratigraphic events.

4.1.2. Age of the P/E Boundary

[64] According to our calibration, the P/E CIE occurred ~0.85 myr following the C24r/C25n reversal. This estimate differs from that of *Aubry et al.* [1996] due primarily to the much shorter duration between the CIE and the base of Zone NP10 obtained in the calibration presented here. By assuming synchrony of the LO of *T. bramlettei*, and thus correlating the NP9/NP10 zonal contacts at Sites 550 and 690, *Aubry et al.* [1996] inferred the presence of a stratigraphic gap at Site 550, thereby artificially extending the upper part of Magnetozone C24r.

[65] Our calibration also differs by ~0.1 myr from the calibration of *Norris and Röhl* [1999], according to which the CIE occurred 0.924–0.966 myr after the beginning of chron C24r (the estimate made by *Cramer* [2001] is consistent with that of *Norris and Röhl* [1999] but is not discussed in detail here because *Cramer* [2001] examined only Hole 1051A and thus had to extrapolate to the position of the CIE). The true difference between the two calibrations in this interval is actually ~0.16 myr because our refined magnetostratigraphy places the C24r/C25n reversal ~1 m below the level used by *Norris and Röhl* [1999] (i.e., according to our calibration the CIE occurred only ~0.78 myr after the point used by *Norris and Röhl* [1999] as the C24r/C25n reversal). The lithologic cyclicity is extraordinarily well defined (Figure 5) and the two cyclostratigraphies are nearly identical between eccentricity maxima C1, C2, and D1. However, in the ~4 m interval immediately below the CIE (within the interval between the CIE and eccentricity maximum D1), there are two intervals where the lithologic cyclicity is disturbed. The upper interval is noted as an intraformational mud clast horizon at the very base of the CIE, as highlighted by *Katz et al.* [1999] (512.82–513.05 mbsf, Core 60X, 42–65 cm, in Hole 1051B [*Shipboard Scientific Party*, 1998]; 512.76–512.98 MCD [*Norris and Röhl*, 1999]). The lower interval shows an alternation of burrow-homogenized sediment and laminated intervals (Figure 10; 515.4–516.58 mbsf, Core 60X, 0–118 cm, in Hole 1051B [*Shipboard Scientific Party*, 1998]; ~515.3–516.5 MCD [*Norris and Röhl*, 1999]). Lamination is not present between this level and the base of Magnetozone C24r; precession cyclicity is instead reflected by smoothly varying lithologic cycles. While *Norris and Röhl* [1999] identified 5–6 cycles (corresponding to laminated/nonlaminated couplets) in the lower interval and 1 cycle in the upper interval, this cannot be made consistent with the eccentricity cycles. Instead, we suggest that each of these intervals was deposited rapidly (in a fraction of a precession cycle) and that only the cyclicity between the two intervals is interpretable as precession-driven.

[66] The number of precession cycles counted by *Norris and Röhl* [1999] is still several more than can be accommodated by the eccentricity-based timescale we present. Similarly, *Dinarès-Turell et al.* [2002] counted 47 presumed precession cycles between the base of chron C24r and the CIE in the outcrop section at Zumaia, Spain, while our calibration would accommodate only 39–41 cycles of 0.021 myr mean duration. Although the mean precession cycle duration was most likely shorter in the early Paleogene than the modern value of 0.021 myr, it is unlikely that this could account for more than 1 extra cycle [e.g., *Berger et al.*, 1992]. We regard our calibration of eccentricity maxima C1, C2, D1, and D2 as very robust, and the number of lithologic cycles that occur between these levels conforms to the eccentricity-based timescale. It is possible that the discrepancy between precession cycle counts and the eccentricity-based timescale indicates that we have underestimated the duration between the CIE and eccentricity maximum C1 or between eccentricity maximum D2 and the base of chron C24r. Alternatively, the excess of lithologic cycles simply reflects errors in discriminating between cycles of precessional origin and lithologic variations resulting from other processes.

[67] The differences in the durations of magnetic polarity chrons presented here and those of *Cande and Kent* [1995] makes assignment of numerical ages to stratigraphic events awkward: calibration relative to one magnetic polarity reversal would produce ages that are inconsistent with the other reversals. The *Cande and Kent* [1992a, 1995] timescale in this interval is ultimately tied to $^{40}Ar/^{39}Ar$ ages for the +19 (54 ± 0.53) and −17 (54.51 ± 0.05) ash layers in the Fur Formation in Denmark. These ashes have been correlated to ashes recovered at Site 550 at 392.98 and 399.87 mbsf, respectively (Figure 4; *Swisher and Knox* [1991]). The orbitally calibrated relative ages for the levels of the two ashes (0.44 myr after the CIE for the +19 ash and 0.24 myr for the −17 ash) is consistent with the duration implied by the $^{40}Ar/^{39}Ar$ ages, although this is not very meaningful given the large analytical error for the age of the +19 ash. Since our orbital calibration places the level of the −17 ash 0.24 myr following the CIE, this implies an age for the CIE of ~54.75 Ma. The error associated with this numerical calibration is not easily quantifiable, as it results from errors in the orbital tuning in this interval at Site 550 (which is very problematic due to coring gaps) and possible errors associated with the ash correlation and $^{40}Ar/^{39}Ar$ date (which was made using an assemblage of grains rather than individual crystals). We therefore strongly caution that the resulting numerical ages should be treated as preliminary; they may be improved through $^{40}Ar/^{39}Ar$ dating of ash layers in situ in an orbitally tuned geologic section and, ultimately, by extension of the orbital timescale from the present.

4.2. Paleoceanographic Implications

[68] The relatively long residence time of carbon necessarily implies a decoupling of $\delta^{13}C$ records from the actual evolution of the carbon cycle on Milankovitch timescales. The smoothing effect of the residence time transfers spectral

power from higher-frequency $\delta^{13}C$ oscillations (e.g., precession) into the eccentricity band, but this effect does not act on actual variations in carbon fluxes. For instance, the eccentricity response observed in the carbon isotope records presented here does not necessarily imply an eccentricity-scale cyclicity in Earth's climate. The eccentricity response should instead be taken as an indication of a robust precessional forcing of the carbon cycle during the late Paleocene–early Eocene. Moreover, the similar amplitude of the eccentricity-scale variations in the $\delta^{13}C$ records presented here and seen in Neogene records [e.g., *Flower and Kennett*, 1995; *Diester-Haass*, 1996; *Zachos et al.*, 1996, 2001b] implies that the sensitivity of the carbon cycle to precessional forcing was similar during warm early Paleogene climates and glacial Neogene climates. It should be emphasized that interpretation of the amplitude of precession-scale features in $\delta^{13}C$ records as a reflection of variability in the carbon cycle must be undertaken with care: the smoothing effect of the residence time diminishes the amplitude of precession-scale changes apparent in $\delta^{13}C$ records relative to actual variations in relative fluxes of carbonate and organic carbon.

4.2.1. Carbon Cycle and Climate Variability

[69] The $\delta^{13}C$ decreases identified in the records presented here occur at eccentricity maxima and therefore provide the basis for predictions about climate variability during the latest Paleocene–earliest Eocene: precessional variability in insolation should be largest at times of eccentricity maxima. Climatic processes at low to mid latitudes should therefore exhibit greatest variability and most rapid change at these times. In order to further investigate this implication, we examined published benthic foraminiferal stable isotope records from Sites 690 and 550. The resolution of the benthic foraminiferal records is poor and aliasing of the underlying Milankovitch signal is a problem, but by plotting them relative to our orbitally tuned chronology the apparent scatter is resolved into a clear pattern showing the influence of orbital forcing (Figure 15).

[70] The eccentricity-controlled transient decreases present in the bulk carbonate $\delta^{13}C$ records are also present in the benthic foraminiferal records, confirming that these events represent changes in the whole ocean carbon reservoir. (We note in passing that the benthic foraminiferal $\delta^{13}C$ records support our identification of eccentricity maxima in the low-amplitude interval above the CIE; Figure 15). In constructing the orbital tuning target for the $\delta^{13}C$ records, we used values for the fraction of carbon deposited as carbonate (f_{carb}) that fluctuate in the range ~0.6–0.9 (Figure 7), producing $\delta^{13}C$ decreases in our target curve that approximately match the amplitude measured in our records (see Figure 8). For comparison, *Hayes et al.* [1999] used measured $\delta^{13}C$ values for carbonates and organic carbon to estimate a value for f_{carb} of ~0.75 in the early Cenozoic. If the standard deviation of 0.05–0.07 calculated for f_{carb} based on the scatter in $\delta^{13}C$ values [*Hayes et al.*, 1999, Table 4] is taken as a reflection of short-term variability in f_{carb}, the variability in the model we use appears to be within, but toward the high end, of the realistic range. We cannot provide similar justification for the relationship between precessional forcing and f_{carb} used in our model, which we emphasize is purely arbitrary. A more complex model would be needed to fully investigate possible explanations for the nonlinear $\delta^{13}C$ response to precession forcing.

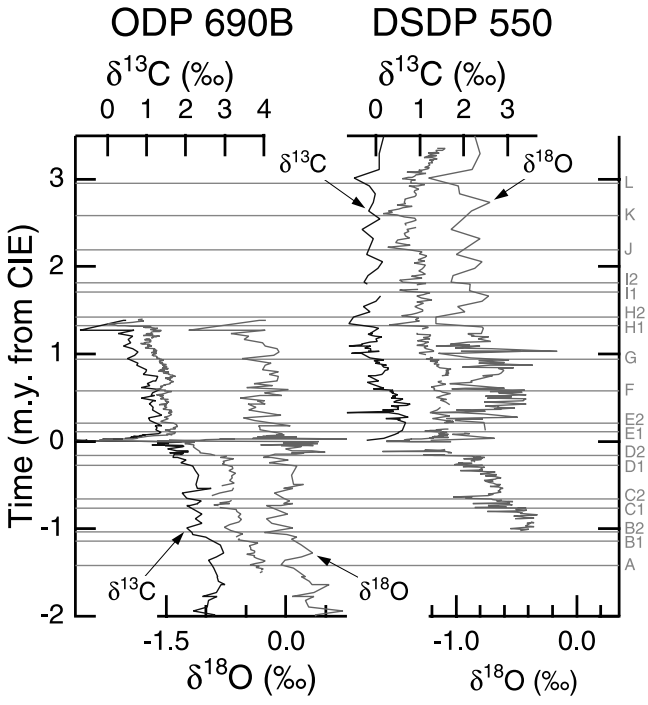

Figure 15. Benthic foraminiferal $\delta^{13}C$ (blue/dark) and $\delta^{18}O$ (red/light) records from Sites 690 [*Kennett and Stott*, 1990], and 550 [*Stott et al.*, 1996; *Charisi and Schmitz*, 1996]. Bulk sediment $\delta^{13}C$ records (this study) are shown in gray for reference. Horizontal lines indicate eccentricity maxima identified in the bulk isotope $\delta^{13}C$ records. Benthic foraminiferal isotope values have been corrected to Cibicidoides spp. using correction factors from *Katz et al.* [2003]. See color version of this figure in the HTML.

[71] The benthic foraminiferal $\delta^{18}O$ records demonstrate a robust deepwater temperature response to orbital forcing of insolation. Of most interest are $\delta^{18}O$ decreases coincident with $\delta^{13}C$ decreases, indicating that deepwater temperatures underwent a rapid 1–4°C temperature increase at each eccentricity maximum (Figure 15). It is possible that the "hyperthermal" rapid warming events postulated by *Thomas et al.* [2000] reflect climate perturbations at eccentricity maxima. We emphasize that, just as the $\delta^{13}C$ transient decreases are the result of precession forcing acting on a process with a long time constant (or "memory"), the $\delta^{18}O$ decreases imply a robust temperature response to precessional variations in insolation in the context of some process that imparts a long time constant (of order 10^4–10^5 years) to climate variations. This is intriguing because it would seem that the time constant would have to be too long to be ascribed to ocean mixing, and the influence of ice sheets (which have generally been implicated as a source of Pleistocene eccentricity-scale $\delta^{18}O$ cycles) on early Paleogene climate is believed to be minimal. The character of precession-scale temperature variations in the early Paleogene clearly requires more detailed investigation.

4.2.2. Implications for the Cause of the CIE

[72] Having confirmed the influence of Earth's orbital eccentricity on late Paleocene–early Eocene climate, we emphasize that the CIE occurred between two long eccentricity maxima (Figure 8). This temporal calibration relative to eccentricity is very robust. It is not possible to shift the CIE so as to make it coincident with a long eccentricity maximum because, as noted above in detail, the integration of precessional cyclicity in the geophysical logs with the carbon isotope records constrains the duration between the preceding (D) and following (E) eccentricity transients to ~400 kyr. Furthermore, we cannot have erred in identifying these two long eccentricity maxima because a duration of ~400 kyr to the next lower (C) and higher (F) eccentricity maxima is also consistent with the precession cyclicity. The data presented here conclusively demonstrate that the CIE occurred near a long eccentricity minimum, in an interval that should be characterized by only low-amplitude changes in $\delta^{13}C$ values.

[73] The position of the CIE with respect to the phase of short (~100 kyr) and very long (~2.4 myr) eccentricity is not as clearly constrained. Because of the large shifts in carbon isotope values associated with the CIE, it is not possible to separate any short eccentricity effect from the major perturbation itself. Thus it is necessary to rely on lithologic cyclicity instead. We refrain from speculation based on the cycle counts presented here since this should properly be done using a comparison of the lithologic variations with a robust calculation of precession variations during this time period, which is presently unavailable. Constraining the phase relative to myr-scale eccentricity cycles presents a very different problem. Our data empirically constrain the CIE to a position somewhere between an older myr-scale eccentricity maximum and a younger minimum, but the uncertainty associated with the actual period of the ~2.4 myr eccentricity component (~±25% as noted above, or a range from ~1.8 to ~3.0 myr) prevents a more precise knowledge of the phase of this component.

[74] The Site 690 and 550 benthic foraminiferal $\delta^{18}O$ records demonstrate that there was a robust deepwater temperature response to precessional forcing of insolation during the late Paleocene–early Eocene, with the highest amplitude response occurring at long eccentricity maxima (Figure 15). Since the CIE and associated rapid warming of the PETM occurred during a minimum in long eccentricity, the temperature response to orbital forcing can be ruled out as a potential trigger for the PETM: any model for such a triggering effect would also have to explain why the PETM was not triggered at the preceding eccentricity maximum. Furthermore, the benthic foraminiferal $\delta^{18}O$ record from Site 690 shows deepwater temperature increases of ~2° C at eccentricity maxima in the 1 myr interval preceding the CIE (Figure 15). Because these temperature responses are accompanied by relatively moderate decreases in $\delta^{13}C$ values, we suggest that thermal dissociation of large quantities of methane hydrate, as has been invoked to explain the CIE, requires an initial temperature increase substantially larger than 2° C. Alternatively, the lack of any clear relationship between orbital variations and the timing of the PETM is entirely consistent with an impact trigger for the event, as suggested by *Kent et al.* [2003].

5. Conclusions

[75] We provide a theoretical justification for the use of carbon isotopes as a proxy for orbital eccentricity. We use a model involving variations in the fraction of carbon deposited as carbonate and organic carbon, but the use of any other control on oceanic $\delta^{13}C$ values that is sensitive to insolation forcing would yield the same result. The importance of the underlying basis for the model presented here should not be underestimated: eccentricity must be present in all carbon isotope records provided that the $\delta^{13}C$ of the net flux of carbon through the ocean-atmosphere-biosphere reservoir responds in a nonlinear fashion to climatic precession. A nonlinear response must be regarded as more likely than a linear response, given the number of variables that contribute to this net flux. The eccentricity signal should be obvious in $\delta^{13}C$ records unless obliquity was overwhelmingly dominant in forcing the carbon cycle, as was the case during the late Neogene. We emphasize that ~1 myr-duration intervals of low-amplitude $\delta^{13}C$ variations are an inherent part of this eccentricity signal, resulting from modulation by myr-scale eccentricity components. Since there is a strong expectation of an eccentricity signal, we suggest that variations in $\delta^{13}C$ records on 10^5-year timescales should be assumed to be orbitally forced until proven otherwise.

[76] Orbital forcing of insolation exerted a dominant control on variability in upper Paleocene–lower Eocene $\delta^{13}C$ records on 10^4–10^6 year timescales. This conclusion should not come as a surprise since Milankovitch forcing has been recognized in climate proxy records throughout the geologic record [e.g., *Hays et al.*, 1976; *Hilgen*, 1991b; *Herbert et al.*, 1995; *Olsen and Kent*, 1996]. However, the amplitude of the orbital imprint on the early Paleogene greenhouse climate has not been fully appreciated: orbitally forced variations in the Paleogene carbon cycle are similar in amplitude to variations in the Neogene.

[77] The Paleocene/Eocene carbon isotope excursion occurred during a minimum in the ~400 kyr eccentricity cycle. This is inconsistent with an orbital trigger for the PETM, although orbital forcing may have influenced the evolution and recovery from the event. Moreover, benthic foraminiferal $\delta^{18}O$ records indicate that there was a robust deepwater temperature response to precessional forcing both before and after the PETM. Therefore we conclude that the timing of the PETM is more consistent with a stochastic process such as a bolide impact and is not the result of a threshold event caused by long-term warming in the late Paleocene–early Eocene.

[78] We have demonstrated the usefulness of using carbon isotope records to constrain both orbital timescale calibrations and cyclostratigraphic correlations. Barring unforeseen complications, we suggest that this method can potentially allow correlation throughout the Cenozoic and for large portions of the Cretaceous with similar precision to that attained in Pleistocene marine sediments. It also allows a

true test of the accuracy of orbital timescales through correlation independent of biostratigraphic and magnetostratigraphic criteria. The resulting orbital calibrations will therefore be more robust than those reliant on precession-scale cyclicity at individual sites.

[79] **Acknowledgments.** We thank J. R. Toggweiler and P. E. Olsen for reviewing the manuscript and Ken Miller, Mimi Katz, Carl Swisher, Bill Berggren, and Kunio Kaiho for discussion and comments that significantly improved this study. This research used samples and data provided by the Ocean Drilling Program (ODP) and we especially thank John Beck for producing copies of the core photographs, Gar Esmay at the East Coast Repository, and Walter Hale and staff at the Bremen Core Repository for help with sampling. This material is based upon work supported under a National Science Foundation (NSF) Graduate Research Fellowship and a Schlanger Ocean Drilling Fellowship from the Joint Oceanographic Institutions (JOI) to B. Cramer while enrolled in a PhD program in the Department of Geological Sciences at Rutgers University. B. Cramer is currently supported under a Postdoctoral Fellowship from the Japan Society for the Promotion of Science (JSPS). LDEO 6555.

References

Ali, J., and E. Hailwood, Magnetostratigraphic (re)calibration of the Paleocene/Eocene boundary interval in Holes 550 and 549, Goban Spur, eastern North Atlantic, *Earth Planet. Sci. Lett.*, *161*, 201–213, 1998.

Ali, J., D. Kent, and E. Hailwood, Magnetostratigraphic reinvestigation of the Palaeocene/Eocene boundary interval in Hole 690B, Maud Rise, Antarctica, *Geophys. J. Int.*, *141*, 639–646, 2000.

Aubry, M.-P., Towards an upper Paleocene-lower Eocene high resolution stratigraphy based on calcareous nannofossil stratigraphy, *Isr. J. Earth Sci.*, *44*, 239–253, 1996.

Aubry, M.-P., Stratigraphic (dis)continuity and temporal resolution in the upper Paleocene-lower Eocene deep sea record, in *Late Paleocene-Early Eocene Climatic and Biotic Events in the Marine and Terrestrial Records*, edited by M.-P. Aubry, S. Lucas, and W. Berggren, pp. 37–66, Columbia Univ. Press, New York, 1998.

Aubry, M.-P., and A. Sanfilippo, Late Paleocene-early Eocene sedimentary history in western Cuba: Implications for the LPTM and for regional tectonic history, *Micropaleontology*, *45*, 5–18, 1999.

Aubry, M.-P., W. Berggren, L. Stott, and A. Sinha, The upper Paleocene-lower Eocene stratigraphic record and the Paleocene-Eocene boundary carbon isotope excursion: Implications for geochronology, in *Correlation of the Early Paleogene in northwest Europe, Special Publication*, vol. 101, edited by R. Knox, R. Corfield, and R. Dunay, pp. 353–380, Geol. Soc., London, 1996.

Aubry, M.-P., C. Requirand, and J. Cook, The *Rhomboaster-Tribrachiatus* lineage: A remarkable succession of events from 55.5 Ma to 53.2 Ma, *GFF*, *122*, 15–18, 2000.

Aubry, M.-P., et al., Proposal: Global standard stratotype-section and point (GSSP) at the Dababyia section (Egypt) for the base of the Eocene series, *Internal Rep.*, Int. Subcommiss. on Paleogene Stratigr., Tübingen, Germany, 2002.

Bains, S., R. Corfield, and R. Norris, Mechanisms of climate warming at the end of the Paleocene, *Science*, *285*, 724–727, 1999.

Berger, A., M. Loutre, and J. Laskar, Stability of the astronomical frequencies over the Earth's history for paleoclimate studies, *Science*, *255*, 560–566, 1992.

Berggren, W., and M.-P. Aubry, A late Paleocene-early Eocene NW European and North Sea magnetobiochronological correlation network, in *Correlation of the Early Paleogene in Northwest Europe, Special Publication*, vol. 101, edited by R. Knox, R. Corfield, and R. Dunay, pp. 309–352, Geol. Soc., London, 1996.

Berggren, W., D. Kent, C. Swisher III, and M.-P. Aubry, A revised Cenozoic geochronology and chronostratigraphy, in *Geochronology, Time Scales and Global Stratigraphic Correlation*, *SEPM Spec. Publ.*, vol. 54, edited by W. Berggren et al., pp. 129–212, Soc. for Sediment. Geol., Tulsa, Okla., 1995.

Bleil, U., The magnetostratigraphy of northwest Pacific sediments, Deep Sea Drilling Project Leg 86, in *Initial Reports of the Deep Sea Drilling Project*, vol. 86, edited by G. Heath, et al., pp. 441–458, U.S. Gov. Print. Off., Washington, D. C., 1985.

Bowen, G., P. Koch, P. Gingerich, R. Norris, S. Bains, and R. Corfield, Refined isotope stratigraphy across the continental Paleocene-Eocene boundary on Polecat Bench in the northern Bighorn Basin, in *Paleocene-Eocene Stratigraphy and Biotic Change in the Bighorn and Clarks Fork Basins, Wyoming*, *Pap. on Paleontol.*, vol. 33, edited by P. Gingerich, pp. 73–88, Mus. of Paleontol., Univ. of Mich., Ann Arbor, 2001.

Bralower, T., J. Zachos, E. Thomas, M. Parrow, C. Paull, D. Kelly, I. Premoli Silva, W. Sliter, and K. Lohmann, Late Paleocene to Eocene paleoceanography of the equatorial Pacific Ocean: Stable isotopes recorded at Ocean Drilling Program Site 865, Allison Guyot, *Paleoceanography*, *10*, 841–865, 1995.

Bralower, T., D. Thomas, J. Zachos, M. Hirschmann, U. Röhl, H. Sigurdsson, E. Thomas, and D. Whitney, High-resolution records of the late Paleocene thermal maximum and circum-Caribbean volcanism: Is there a causal link?, *Geology*, *25*, 963–966, 1997.

Broecker, W., and T.-H. Peng, *Tracers in the Sea*, 690 pp., Lamont-Doherty Geol. Observ., Palisades, N. Y., 1982.

Cande, S., and D. Kent, A new geomagnetic polarity timescale for the Late Cretaceous and Cenozoic, *J. Geophys. Res.*, *97*, 13,917–13,951, 1992a.

Cande, S., and D. Kent, Ultrahigh resolution marine magnetic anomaly profiles: A record of continuous paleointensity variations?, *J. Geophys. Res.*, *97*, 15,075–15,083, 1992b.

Cande, S., and D. Kent, Revised calibration of the geomagnetic polarity timescale for the Late Cretaceous and Cenozoic, *J. Geophys. Res.*, *111*, 6093–6095, 1995.

Charisi, S., and B. Schmitz, Early Eocene palaeoceanography and palaeoclimatology of the eastern North Atlantic: Stable isotope results for DSDP Hole 550, in *Correlation of the Early Paleogene in Northwest Europe*, *Special Publication*, vol. 101, edited by R. Knox, R. Corfield, and R. Dunay, pp. 457–472, Geol. Soc., London, 1996.

Cramer, B., Latest Paleocene-earliest Eocene cyclostratigraphy: Using core photographs for reconnaissance geophysical logging, *Earth Planet. Sci. Lett.*, *186*, 231–244, 2001.

Cramer, B., M.-P. Aubry, K. Miller, R. Olsson, J. Wright, and D. Kent, An exceptional chronologic, isotopic, and clay mineralogic record of the latest Paleocene thermal maximum, Bass River, NJ, ODP 174AX, *Bull. Soc. Geol. Fr.*, *170*, 883–897, 1999.

Dickens, G., J. O'Neil, D. Rea, and R. Owen, Dissociation of oceanic methane hydrate as a cause of the carbon isotope excursion at the end of the Paleocene, *Paleoceanography*, *10*, 965–971, 1995.

Dickens, G., M. Castillo, and J. Walker, A blast of gas in the latest Paleocene: Simulating first-order effects of massive dissociation of oceanic methane hydrate, *Geology*, *25*, 259–262, 1997.

Diester-Haass, L., Late Eocene-Oligocene paleoceanography in the southern Indian Ocean (ODP Site 744), *Mar. Geol.*, *130*, 99–119, 1996.

Dinarès-Turell, J., J. Baceta, V. Pujalte, X. Orue-Etxebarria, and G. Bernaola, Magnetostratigraphic and cyclostratigraphic calibration of a prospective Palaeocene/Eocene stratotype at Zumaia (Basque Basin, northern Spain), *Terra Nova*, *14*, 371–378, 2002.

Farley, K., and S. Eltgroth, An alternative age model for the Paleocene-Eocene thermal maximum using extraterrestrial ^{3}He, *Earth Planet. Sci. Lett.*, *208*, 135–148, 2003.

Flower, B., and J. Kennett, Middle Miocene deepwater paleoceanography in the southwest Pacific: Relations with East Antarctic Ice Sheet development, *Paleoceanography*, *10*, 1095–1112, 1995.

Gee, J. S., and S. C. Cande, A surface-towed vector magnetometer, *Geophys. Res. Lett.*, *29*(14), 1670, doi:10.1029/2002GL015245, 2002.

Ghil, M., et al., Advanced spectral methods for climatic time series, *Rev. Geophys.*, *40*(1), 1003, doi:10.1029/2000RG000092, 2002.

Hay, W., et al., Alternative global Cretaceous paleogeography, in *The Evolution of Cretaceous Ocean/Climate Systems*, *Geol. Soc. Am. Spec. Pap.*, vol. 332, edited by E. Barrera and C. Johnson, pp. 1–47, Geol. Soc. of Am., Boulder, Colo., 1999.

Hayes, J., H. Strauss, and A. Kaufman, The abundance of ^{13}C in marine organic matter and isotopic fractionation in the global biogeochemical cycle of carbon during the past 800 ma, *Chem. Geol.*, *161*, 103–125, 1999.

Hays, J., J. Imbrie, and N. Shackleton, Variations in the Earth's orbit: Pacemaker of the ice ages, *Science*, *194*, 1121–1133, 1976.

Herbert, T., I. Premoli Silva, E. Erba, and A. Fischer, Orbital chronology of Cretaceous-Paleocene marine sediments, in *Geochronology, Time Scales and Global Stratigraphic Correlation*, *SEPM Spec. Publ.*, vol. 54, edited by W. Berggren et al., pp. 81–92, Soc. for Sediment. Geol., Tulsa, Okla., 1995.

Hilgen, F., Astronomical calibration of Gauss to Matuyama sapropels in the Mediterranean and

implication for the geomagnetic polarity time scale, *Earth Planet. Sci. Lett.*, *104*, 226–244, 1991a.

Hilgen, F., Extension of the astronomically calibrated (polarity) time scale to the Miocene/Pliocene boundary, *Earth Planet. Sci. Lett.*, *107*, 349–368, 1991b.

Kaiho, K., et al., Latest Paleocene benthic foraminiferal extinction and environmental changes at Tawanui, New Zealand, *Paleoceanography*, *11*, 447–465, 1996.

Katz, M., D. Pak, G. Dickens, and K. Miller, The source and fate of massive carbon input during the latest Paleocene thermal maximum, *Science*, *286*, 1531–1533, 1999.

Katz, M. E., D. R. Katz, J. D. Wright, K. G. Miller, D. K. Pak, N. J. Shackleton, and E. Thomas, Early Cenozoic benthic foraminiferal isotopes: Species reliability and interspecies correction factors, *Paleoceanography*, *18*(2), 1024, doi:10.1029/2002PA000798, 2003.

Kennett, J., and L. Stott, Proteus and Proto-Oceanus: Ancestral Paleogene oceans as revealed from Antarctic stable isotopic results; ODP Leg 113, *Proc. of the Ocean Drill. Program Sci. Results*, *113*, 865–880, 1990.

Kennett, J., and L. Stott, Abrupt deep-sea warming, palaeceanographic changes and benthic extinctions at the end of the Palaeocene, *Nature*, *353*, 225–229, 1991.

Kent, D., B. Cramer, L. Lanci, D. Wang, J. Wright, and R. Van der Voo, A case for a comet impact trigger for the Paleocene/Eocene thermal maximum and carbon isotope excursion, *Earth Planet. Sci. Lett.*, *211*, 13–26, doi:10.1016/S0012-821X(03)00188-2, 2003.

Koch, P., J. Zachos, and P. Gingerich, Correlation between isotope records in marine and continental carbon reservoirs near the Palaeocene/Eocene boundary, *Nature*, *358*, 319–322, 1992.

Koch, P., J. Zachos, and D. Dettman, Stable isotope stratigraphy and paleoclimatology of the Paleogene Bighorn Basin (Wyoming, USA), *Palaeogeogr. Palaeoclimatol. Palaeoecol.*, *115*, 61–89, 1995.

Kump, L., and M. Arthur, Interpreting carbon-isotope excursions: Carbonates and organic matter, *Chem. Geol.*, *161*, 181–198, 1999.

Laskar, J., The chaotic motion of the Solar System: A numerical estimate of the size of the chaotic zones, *Icarus*, *88*, 266–291, 1990.

Laskar, J., The limits of Earth orbital calculations for geological time-scale use, *Philos. Trans. R. Soc. London A*, *357*, 1735–1759, 1999.

Lourens, L., and F. Hilgen, Long-periodic variations in the Earth's obliquity and their relation to third-order eustatic cycles and Late Neogene glaciations, *Quat. Int.*, *40*, 43–52, 1997.

Martini, E., Standard Tertiary and Quaternary calcareous nannoplankton zonation, in *Proceedings of the Second Planktonic Conference, Rome*, edited by A. Farinacci, pp. 739–761, Edizioni Technosci., Rome, 1971.

Martinson, D., W. Menke, and P. Stoffa, An inverse approach to signal correlation, *J. Geophys. Res.*, *87*, 4807–4818, 1982.

Maslin, M., X. Li, M.-F. Loutre, and A. Berger, The contribution of orbital forcing to the progressive intensification of Northern Hemisphere glaciation, *Quat. Sci. Rev.*, *17*, 411–426, 1998.

Mead, G., Correlation of Cenozoic-Late Cretaceous geomagnetic polarity timescales: An Internet archive, *J. Geophys. Res.*, *101*, 8107–8109, 1996.

Miller, K., and R. Fairbanks, Oligocene to Miocene carbon isotope cycles and abyssal circulation changes, in *The Carbon Cycle and Atmospheric CO_2: Natural Variations Archean to Present*, *Geophys. Monogr. Ser.*, vol. 32, edited by E. Sundquist and W. Broecker, pp. 469–486, AGU, Washington, D. C., 1985.

Miller, K., R. Fairbanks, and G. Mountain, Tertiary oxygen isotope synthesis, sea level history, and continental margin erosion, *Paleoceanography*, *2*, 1–19, 1987.

Mita, I., Data report: Early to late Eocene calcareous nannofossil assemblages of Sites 1051 and 1052, Blake Nose, northwestern Atlantic Ocean, *Proc. Ocean Drill. Program Sci. Results*, *171B*, 1–28, 2001.

Monechi, S., Campanian to Pleistocene calcareous nannofossil stratigraphy from the northwest Pacific Ocean, Deep Sea Drilling Project Leg 86, *Initial Rep. Deep Sea Drill. Project*, *86*, 301–336, 1985.

Muller, C., Biostratigraphic and paleoenvironmental interpretation of the Goban Spur region based on a study of calcareous nannoplankton, *Initial Rep. Deep Sea Drill. Project*, *80*, 389–414, 1985.

Norris, R., and U. Röhl, Carbon cycling and chronology of climate warming during the Palaeocene/Eocene transition, *Nature*, *401*, 775–778, 1999.

Ogg, J., and L. Bardot, Aptian through Eocene magnetostratigraphic correlation of the Blake Nose Transect (Leg 171B), Florida continental margin, *Proc. of the Ocean Drill. Program Sci. Results*, *171BB*, 1–58, 2001.

Olsen, P., and D. Kent, Milankovitch climate forcing in the tropics of Pangaea during the Late Triassic, *Palaeogeogr. Palaeoclimatol. Palaeoecol.*, *122*, 1–26, 1996.

Olsen, P., and D. Kent, Long-period Milankovitch cycles from the Late Triassic and Early Jurassic of eastern North America and their implications for the calibration of the Early Mesozoic time-scale and the long-term behaviour of the planets, *Philos. Trans. R. Soc. London A*, *357*, 1761–1786, 1999.

Pospichal, J., and S. Wise, Paleocene to middle Eocene calcareous nannofossils of ODP Sites 689 and 690, Maud Rise, Weddell Sea, *Proc. Ocean Drill. Program Sci. Results*, *113*, 613–666, 1990.

Röhl, U., T. Bralower, R. Norris, and G. Wefer, New chronology for the late Paleocene thermal maximum and its environmental implications, *Geology*, *28*, 927–930, 2000.

Sarmiento, J., and M. Bender, Carbon biogeochemistry and climate-change, *Photosyn. Res.*, *39*, 209–234, 1994.

Schmitz, B., R. Speijer, and M.-P. Aubry, Latest Paleocene benthic extinction event on the southern Tethyan shelf (Egypt): Foraminiferal stable isotopic ($\delta^{13}C$, $\delta^{18}O$) records, *Geology*, *24*, 347–350, 1996.

Shackleton, N., The carbon isotope record of the Cenozoic: History of organic carbon burial and of oxygen in the ocean and atmosphere, in *Marine Petroleum Source Rocks*, *Geol. Soc. Spec. Publ.*, vol. 26, edited by J. Brooks, and A. Fleet, pp. 423–434, Geol. Soc., London, 1987.

Shackleton, N., The 100,000-year ice-age cycle identified and found to lag temperature, carbon dioxide, and orbital eccentricity, *Science*, *289*, 1897–1902, 2000.

Shackleton, N., M. Hall, and U. Bleil, Carbon-isotope stratigraphy, Site 577, *Initial Rep. Deep Sea Drill. Project*, *86*, 503–511, 1985.

Shackleton, N., A. Berger, and W. Peltier, An alternative astronomical calibration of the lower Pleistocene timescale based on ODP Site 677, *Trans. R. Soc. Edinburgh Earth Sci.*, *81*, 251–261, 1990.

Shackleton, N., S. Crowhurst, G. Weedon, and J. Laskar, Astronomical calibration of Oligocene-Miocene time, *Philos. Trans. R. Soc. London*, *357*, 1907–1929, 1999.

Shackleton, N., M. Hall, I. Raffi, L. Tauxe, and J. Zachos, Astronomical calibration age for the Oligocene-Miocene boundary, *Geology*, *28*, 447–450, 2000.

Shipboard Scientific Party, Site 1051, *Proc. Ocean Drill. Program Initial Rep.*, *171B*, 171–239, 1998.

Siegenthaler, U., and J. Sarmiento, Atmospheric carbon dioxide and the ocean, *Nature*, *365*, 119–125, 1993.

Stott, L., and J. Kennett, Antarctic Paleogene planktonic foraminifer biostratigraphy: ODP Leg 113, Sites 689 and 690, *Proc. Ocean Drill. Program Sci. Results*, *113*, 549–562, 1990.

Stott, L., A. Sinha, M. Thiry, M.-P. Aubry, and W. Berggren, Global $\delta^{13}C$ changes across the Paleocene-Eocene boundary: Criteria for terrestrial-marine correlations, in *Correlation of the Early Paleogene in Northwest Europe*, *Special Publication*, vol. 101, edited by R. Knox, R. Corfield, and R. Dunay, pp. 381–399, Geol. Soc., London, 1996.

Swisher, C., III, and R. Knox, The age of the Paleocene/Eocene boundary: $^{40}Ar/^{39}Ar$ dating of the lower part of NP10, North Sea Basin and Denmark, in *International Annual Meeting and Field Conference*, *2–6 December 1991*, *Brussels*, *Abstracts With Program*, p. 16, IGCP 308 Paleocene/Eocene boundary events, 1991.

Tarling, D., and J. Mitchell, Revised Cenozoic polarity time scale, *Geology*, *4*, 133–136, 1976.

Thomas, D., T. Bralower, and J. Zachos, New evidence for subtropical warming during the late Paleocene thermal maximum: Stable isotopes from Deep Sea Drilling Project Site 527, Walvis Ridge, *Paleoceanography*, *14*, 561–570, 1999.

Thomas, D., J. Zachos, T. Bralower, E. Thomas, and S. Bohaty, Warming the fuel for the fire: Evidence for the thermal dissociation of methane hydrate during the Paleocene-Eocene thermal maximum, *Geology*, *30*, 1067–1070, 2002.

Thomas, E., and N. Shackleton, The Paleocene-Eocene benthic foraminiferal extinction and stable isotope anomalies, in *Correlation of the Early Paleogene in Northwest Europe, Special Publication*, vol. 101, edited by R. Knox, R. Corfield, and R. Dunay, pp. 401–441, Geol. Soc., London, 1996.

Thomas, E., J. Zachos, and T. Bralower, Deep-sea environments on a warm earth: Latest Paleocene-early Eocene, in *Warm Climates in Earth History*, edited by B. Huber, K. MacLeod, and S. Wing, pp. 132–160, Cambridge Univ. Press, New York, 2000.

Townsend, H., The paleomagnetism of sediment acquired from the Goban Spur on Deep Sea Drilling Project Leg 80, *Initial Rep. Deep Sea Drill. Project*, *80*, 389–414, 1985.

Vincent, E., and W. Berger, Carbon dioxide and polar cooling in the Miocene: The Monterey Hypothesis, in *The Carbon Cycle and Atmospheric CO_2: Natural Variations Archean to Present*, *Geophys. Monogr. Ser.*, vol. 32, edited

by E. Sundquist and W. Broecker, pp. 455–468, AGU, Washington, D. C., 1985.

Woodruff, F., and S. Savin, Mid-Miocene isotope stratigraphy in the deep sea: High-resolution correlations, paleoclimatic cycles, and sediment preservation, *Paleoceanography*, *6*, 755–806, 1991.

Zachos, J., K. Lohmann, J. Walker, and S. Wise, Abrupt climate change and transient climates during the Paleogene: A marine perspective, *J. Geol.*, *101*, 191–213, 1993.

Zachos, J., T. Quinn, and K. Salamy, High-resolution (10^4 years) deep-sea foraminiferal stable isotope records of the Eocene-Oligocene climate transition, *Paleoceanography*, *11*, 251–266, 1996.

Zachos, J., B. Flower, and H. Paul, Orbitally paced climate oscillations across the Oligocene/Miocene boundary, *Nature*, *388*, 567–570, 1997.

Zachos, J., M. Pagani, L. Sloan, E. Thomas, and K. Billups, Trends, rhythms, and aberrations in global climate 65 Ma to Present, *Science*, *292*, 686–693, 2001a.

Zachos, J., N. Shackleton, J. Revenaugh, H. Päliken, and B. Flower, Climate response to orbital forcing across the Oligocene-Miocene Boundary, *Science*, *292*, 274–278, 2001b.

M.-P. Aubry, D. V. Kent, and J. D. Wright, Department of Geological Sciences, Rutgers University, Piscataway, NJ 08854-8066, USA. (aubry@rci.rutgers.edu; dvk@rci.rutgers.edu; jdwright@rci.rutgers.edu)

B. S. Cramer, Institute of Geology and Paleontology, Tohoku University, Aoba, Aramaki, Sendai 980-8578, Japan. (benjamin@dges.tohoku.ac.jp)